Powering a Giant: Using X-ray Emission to Determine the Power Source of Ultraluminous Infrared Galaxies

by

Jennifer K. Beanlands

A THESIS SUBMITTED IN PARTIAL FULFILMENT OF
THE REQUIREMENTS FOR THE DEGREE OF

BACHELOR OF SCIENCE

in

Honours Astrophysics

(Department of Astronomy and Physics, Dr. Luigi Gallo supervising faculty)

.....
.....
.....
.....
.....

SAINT MARY'S UNIVERSITY

April 25, 2013

Abstract

Powering a Giant: Using X-ray Emission to Determine the Power Source of Ultraluminous Infrared Galaxies

by *Jennifer K. Beanlands*

submitted on April 25, 2013:

Ultraluminous Infrared Galaxies (ULIRGs) are one of the brightest sources of infrared radiation in the Universe, with luminosities upwards of 10^{12} times that of the Sun. To produce the extreme infrared luminosity found in these dusty galaxies, it is thought that they are powered by starbursts, Active Galactic Nuclei (AGN), or a combination of both. Because these galaxies contain a large amount of dust, most of the defining characteristics are obscured, making it difficult to identify the nature of the power source. High energy X-rays are able to penetrate much of the obscuring gas and dust, and potentially reveal the power source. Both AGN and starburst emission produce very specific X-ray spectra, which means that it should be possible to distinguish between the two by examining only the 0.5 to 10.0keV spectral range of specific ULIRGs. To do this, spectra between 0.5 and 10.0keV were created for a sample of eleven ULIRGs from observations made by the space-based telescope, *XMM-Newton*. The X-ray spectra were fitted with starburst and AGN models using the `Xspec` software. Most of the objects appear to be starburst driven, although a significant fraction seem to host an AGN.

Contents

Contents . . . iii

List of Figures . . . vi

List of Tables . . . viii

1 Introduction . . . 1

1.1 A Central Power Source . . . 1

1.2 The Use of X-rays . . . 2

1.3 Active Galactic Nuclei . . . 3

1.4 Starburst . . . 4

2 Galaxy Sample . . . 6

3 Instrumentation . . . 8

3.1 pn-CCD Detector . . . 8

4 Tools for Data Analysis . . . 11

4.1 Science Analysis Software . . . 11

4.2 Xspec . . . 11

4.3 Models . . . 12

4.3.1 `Tbabs` & `Ztbabs` . . . 12

4.3.2 ZPCFABS 13

4.3.3 ZXIPCF 13

4.3.4 ZBBODY 15

4.3.5 MEKAL 16

4.3.6 ZPOWERLW 17

4.3.7 ZGAUSS 18

5 Spectral Analysis and Classification 19

5.1 IRAS F08572-3915 21

5.2 IRAS F14348-1447 22

5.3 Arp 220 23

5.4 Mrk 231 24

5.5 IRAS F10565+2448 25

5.6 IRAS F15250+3608 26

5.7 UGC 5101 27

5.8 IRAS F12112+0305 28

5.9 Mrk 273 29

5.10 IRAS F22491-1808 30

5.11 IRAS F05189-2524 31

5.12 Luminosity 33

6 Classification 35

6.1 Model Components 36

7 Graphical Analysis 41

7.1 Thermal and Power Law Luminosities 41

7.2 Infrared and power law luminosities. 42

7.3 Infrared and Thermal Luminosities 43

7.4 Thermal and Power Law to Infrared Luminosity Ratios . 44

8 Hard X-ray Emission in Starburst Galaxies 46

8.1 The Presence of High Mass X-ray Binaries 46

8.1.1 Star Formation Rate 47

9 Summary 51

Bibliography 53

List of Figures

4.1 Partial Covering Model. In both the neutral and ionized partial covering models, a medium is partially obstructing the X-ray source. In these cases, the observer will see some of the direct light from the source and some light that has been absorbed and re-emitted by the medium in the direction of the observer. Much of the light through the medium will be scattered elsewhere. 14

5.1 Modeled spectra of Mrk 231 between 2.0 and 10.0 keV 20

5.2 IRAS F08572-3915: Mekal and Power Law 22

5.3 IRAS F14348-1447: Absorbed Mekal and Power Law 23

5.4 Arp 220: Mekal and Power Law 24

5.5 Mrk 231: Absorbed Blackbody and Power Law 25

5.6 IRAS F10565+2448: Mekal and Power Law model with a Neutral Partial Covering 26

5.7 IRAS F15250+3608: Absorbed Mekal and Power Law 27

5.8 UGC 5101: Absorbed Blackbody and Power Law 28

5.9 F12112+0305: Mekal and Power Law model with a Neutral Partial Covering 29

5.10 Mrk 273: Mekal and Power Law model with an Ionized Partial Covering 30

5.11 IRAS F22491-1808: Absorbed Mekal and Power Law 31

5.12 IRAS F05189-2524: Mekal With an Ionized Partial Covering and Absorbed Power law 32

6.1 Mrk 231. Classified as containing an AGN, the components of the modeled spectra are shown. The power law is shown in red, the blackbody emission in blue, and the iron line in green. 38

6.2 Arp 220. Classified as dominated by starburst emission, the components of the modeled spectra are shown. The power law is shown in red, the mekal emission in blue, and the iron line in green. 39

6.3 Mrk 273. Classified as blended, the components of the modeled spectra are shown. The power law is shown in red, the mekal emission in blue, and the two iron lines in green. 40

7.1 Best fit thermal and power law luminosities of classified ULIRGs. The red Squares represent AGN, the green circles represent starburst dominated galaxies and the black diamonds represent blended galaxies. . 42

7.2 Infrared and power law luminosities of classified ULIRGs. 43

7.3 Best fit infrared and thermal luminosities of classified ULIRGs 44

7.4 Infrared and thermal luminosities of classified ULIRGs. 45

8.1 Infrared and power law star formation rates of local ULIRGs. 49

List of Tables

2.1 Properties of Local ULIRG Sample 7

3.1 X-ray Observation Log 9

5.1 Properties of the ULIRG Sample 21

5.2 Luminosities of the Model Components 34

6.1 Classified Galaxies 37

Chapter 1

INTRODUCTION

The launch of the Infrared Astronomical Satellite (IRAS) in 1983 enabled the first all-sky survey at infrared wavelengths and provided observations of approximately 250,000 objects. One of the important discoveries of this survey was the first observations in large numbers of a relatively new class of galaxy with extremely high infrared luminosities. Defined as having infrared luminosities of $L_{IR} \geq 10^{12} L_{\odot}$, these aptly-named Ultraluminous Infrared Galaxies (ULIRGs) are considered to be the brightest sources of infrared radiation in the universe, and are comparable to optically bright quasars. Although the source of this extreme luminosity is not fully understood, the theories of extreme starburst activity or an active galactic nucleus (AGN), or some combination of both, are considered likely sources for this emission.

1.1 A Central Power Source

Two important properties of ULIRGs are that they are generally thought to be formed through mergers of gas rich galaxies and, while rare locally[1], they are much more common at higher redshifts. Furthermore, some studies have argued that high redshift ULIRGs may be a very early form of what we now see as large elliptical and lenticular galaxies (Francschini et al., 2003). This concept of evolution of galaxies may be linked

[1]locally is defined here as being z¡1

to understanding their power source. Thus, a determination of the interior structure of these galaxies could provide insight into the formation and evolution of some galaxies, as well as improve our understanding of the nature of AGNs and what triggers them. It is unfortunate however, that the unusually large column densities (nH) associated with these galaxies tend to be centred around the nucleus (Lonsdale, Farrah & Smith, 2006) making them optically thick at most wavelengths and obscuring the majority of the defining characteristics.

1.2 The Use of X-rays

One benefit of observing objects at high energies is that high-energy photons are able to penetrate large columns of obscuring gas and dust. Therefore, so long as the object in question has a sufficiently large X-ray flux, the emission at these wavelengths should provide a better understanding of what hidden processes are taking place. Because starburst and AGN have sufficiently unique X-ray spectra, it should also be possible to differentiate between the two by observing their high energy emission.

The difficulty with using X-rays to observe the inner structure of these galaxies is that ULIRGs are intrinsically dim even at high energies. The galaxies are so dusty and with such high star formation rates, that there is a significant drop in the intensity of even high energy photons leaving the galaxies. It wasnt until the launch of telescopes with large collecting areas like *Chandra* and *XMM-Newton*, that sufficiently detailed X-ray spectra for these galaxies were obtained.

1.3 Active Galactic Nuclei

Active galactic nuclei (AGN) are large, rapidly accreting, supermassive black holes found at the centre of some galaxies. They are extremely energetic objects which, although less than a parsec in size, have the potential to produce jets[2] which can be many times larger than the diameter of the host galaxy. The energy generated by these objects is widely accepted as being the product of friction within an accretion disk around the supermassive black hole (those with masses upwards of $\geq 10^5 M_{\odot}$). The amount of radiation generated from the accretion disk is enough to heat the gas and dust (either circumnuclear or in the larger host galaxy), making it a possible candidate for the source of the extreme infrared luminosities associated with ULIRGs.The accretion disk itself radiates like a blackbody, and peaks in the ultraviolet range of the electromagnetic spectrum. This energy is absorbed by the cool gas and dust and then re-radiated at infrared wavelengths, similar to that in starburst galaxies (see section 1.4)

One of the defining characteristics of AGN activity is the presence of a specific X-ray spectrum. Although not directly formed in the accretion disk, lower energy UV photons emitted from the disk via blackbody radiation are up-scattered to X-rays by relativistic electrons in the corona. This process is known as Comptonization, or inverse Compton scattering, and produces a power law spectrum. While the disk itself emits like a blackbody, it is responsible for the most prominent narrow line feature in the spectrum - that of iron emission. The neutral Fe Kα emission line is seen at

[2]Jets are seen in some but not all AGN. They have not been documented in ULIRGs.

around 6.4 keV and is a strong feature because of its abundance and high fluorescent yield, C_k. This line is usually accredited to the distant tourus, or other dusty regions in ULIRGs.

1.4 STARBURST

Starburst galaxies defined as a galaxy undergoing a rapid rate of star formation as compaired to the long term star formation rate of the galaxy. In ULIRGs specifically, the star formation rates tend to be in excess of 1000 $M_{\odot}\ yr^{-1}$ (Farrah et al., 2008). These galaxies are associated with a high gas and dust content, and tend to show signs of tidal forces from interactions with other galaxies. While their emission generally peaks in the infrared, the source of the radiation is originally emitted at ultraviolet and optical wavelengths from the young, hot stars characteristic of these galaxies. These higher energy photons are absorbed by the cool dust particles surrounding the star formation and are re-radiated as infrared radiation, which means that starburst activity could also explain the luminosities found in ULIRGs.

Also contributing to the infrared spectrum is emission by Polycyclic Aromatic Hydrocarbons (PAHs), which are a component of the gas and dust. When heated by the young stars, the PAHs produce broad line features most promenently at 0.20, 1.61, 1.44, 0.11 and 0.09 eV (Desai et al., 2007). The strong radiation fields associated with AGNs destroy the PAH molecules, and therefor AGN dominated ULIRGs tend to have smaller PAH line to continuum ratios than those dominated by starburst emission (Lonsdale, Farrah & Smith, 2006). As this study looked at X-ray emission,

the PAH ratios in the sample galaxies were not considered.

Along with the infrared component of the spectrum, starburst galaxies produce soft X-ray emission between 0.5 and 2.0 keV. Although far less luminous than the infrared radiation, the hot plasmas associated with star formation produce thermal bremsstrahlung radiation which is distinct from the X-ray emission produced by an AGN. This emission is thought to be the product of interactions between the cooler, dense, interstellar medium and the hot super-winds (Strickland, Heckman, Weaver & Dalhem, 2000) generated by supernovae and stellar winds (Heckman, Lehnert & Armus, 1993). The interstellar medium (ISM) is heated by these super-winds through a combination of shock waves, hydrodynamical mixing and/or cloud evaporation. Narrow features such as iron lines at around 6.7 and 6.97 keV may be also be observed in the spectra because of their association with hot thermal plasmas. While it is also possible for these features to be observed in AGN powered ULIRGs, it is much more probable in starburst driven galaxies.

Chapter 2

Galaxy Sample

This study fucuses on determining the power source of eleven local ULIRGs by investigating their X-ray emission. The eleven galaxies were selected from a larger study that investigated the spectral distribution of 64 local Luminous Infrared Galaxies ($L_{IR} \geq 10^{11} L_{\odot}$) (Vivian et al., 2012). The galaxies selected were considered to be ULIRGs, i.e. with infrared luminosities greater than $10^{12} L_{\odot}$. The properties of each galaxy are outlined in Table 2.1.

The objects in the study by Vivian et al. (2012) were chosen as a subset of the *IRAS* Bright Galaxy Sample, and included all galaxies with infrared luminosities greater than $10^{11.14} L_{\odot}$. The galaxies chosen were also limited by having a Galactic latitude of $b > |30°|$ to reduce Galactic extinction, and a declination of $\delta > -30°$ so they could be observed at Mauna Kea (Vivian et al., 2012). This means that the sample of eleven ULIRGs in this study includes 50% of all galaxies in the Great Observatories All-sky LIRG Survey (Armus et al., 2009).

It is important to note that all of the galaxies in the sample for this study had redshifts less than 0.8. Becasue of different morphologies and the potential for different origins of ULIRGs at higher redshifts (see section 1.1), it is important to consider distances when chosing a sample. With all of the selected ULIRGs being relatively local, it is safe to assume that the galaxies in this study have a similar origin and

Table 2.1: Properties of Local ULIRG Sample

Object	Right Assention [a] (J2000)	Declination[a] (J2000)	Redshift(z)	Galactic nH (10^{20} cm^{-2})	L_{FIR} (10^{45} ergs^{-1})
IRAS F05189-2524	05 21 01.5	-25 21 45	0.042563	1.66	5.549
IRAS F08572-3915	09 00 25.4	+39 03 54	0.058350	2.02	5.549
IRAS F10565+2448	10 59 18.1	+24 32 35	0.043100	1.07	4.615
IRAS F12112+0305	12 13 46.0	+02 48 38	0.073317	1.81	8.795
UGC 5101	09 35 51.6	+61 21 11	0.039367	3.00	3.928
IRAS F14348-1447	14 37 38.3	-15 00 23	0.083000	7.54	9.424
IRAS F15250+3608	15 26 59.4	+35 58 38	0.055155	1.49	4.615
IRAS F22491-1808	22 51 49.1	-17 52 23	0.077760	2.28	6.084
Mrk 231	12 56 14.2	+56 52 25	0.042170	0.964	1.426
Mrk 273	13 44 42.1	+55 53 13	0.037780	0.890	6.226
Arp 220	15 34 57.1	+23 30 11	0.018126	3.90	7.315

[a]Values taken from Vivian et al. (2012)

morphology, making the sample unbiased towards both morphologies and evolution.

As in the original larger study, a Hubble constant of $H_0 = 70 \text{kms}^{-1}\text{Mpc}^{-1}$ has been assumed.

Chapter 3

Instrumentation

The eleven galaxies in the sample were observed using the European Space Agency's space-based telescope, *XMM-Newton*. The telescope was launched in 1999, and is ideal for observing ULIRGs becasue of its large collecting area. *XMM-Newton* has three telescopes with 58 Wolter I grazing-incidence mirrors in each and a gold reflective coating. The highly eliptical orbit means that it ranges from 150,000 to 6000 km from the earth's surface in one orbit (XMM-Newton Users Handbook, 2012).

3.1 pn-CCD Detector

The data for the objects were obtained using the pn-CCD detector, which is part of *XMM-Newton*'s European Photon Imaging Camera (EPIC). Originally developed at the Max-Planck Institute for Physics(Popp et al., 1998), the design is rather straightforward. As X-ray photons hit the surface of the silicone material used in the detector, electrons are released at a rate proportional to the energy of the incident photon. The electrons are removed using a strong magnetic field, and are read out as an event. The detector itself consists of 12 smaller CCDs combined into one larger system with a 4.1 arc sec resolution (Popp et al., 1998)

Although the pn-CCD detector is considered to be efficient from between 0.13 and 15 keV(Popp et al., 1998), poor calibration, background and detector noise tend

Table 3.1: X-ray Observation Log

Object	Observation ID	Rev.	Observation Date	Duration (10^4s)	pn Window Mode	Filter	GTI (10^4s)
IRAS F05189-2524	0085640101	233	2001-3-17 19:06:37.00	1.231	prime full	thin 1	0.646
IRAS F08572-3915	0200630101	796	2004-04-13 23:05:58	2.8918	prime full	thin 1	1.435
IRAS F10565+2448	0150320201	645	2003-06-17 15:06:21.00	3.2217	prime full	thin 1	2.618
IRAS F12112+0305	0081340801	377	201-12-30 11:47:23	2.3068	prime full	thin 1	1.792
UGC 5101	0085640201	353	2001-11-12 08:55:54	3.4957	prime full extended	thin 1	2.651
IRAS F14348-1447	0081341401	483	2002-07-29 21:22:36	2.1892	prime full	medium	1.607
IRAS F15250+3608	0081341101	404	2002-02-22 16:57:45	2.002	prime full	thin 1	1.53
IRAS F22491-1808	0081340901	267	2001-05-24 19:23:12	2.3209	prime full	medium	1.79
Mrk 231	008340201	274	2001-06-07 13:15:44	2.2342	prime full	medium	1.721
Mrk 273	0101640401	441	2005-05-01 03:58:56	2.284	prime full	thick	1.797
Arp 220	0101640801	489	2002-08-11 08:39:10	1.3974	prime full	medium	1.081
	0101640901	568	2003-01-16 20:07:31	1.4865	prime full	medium	0.8342
	020550201	934	2005-01-14 22:20:13	3.5286	prime full	medium	0.6705
	0205510401	952	2005-02-19 21:04:44	2.9008	prime full	medium	0.4265
	0205510501	956	2005-02-27 21:02:41	2.9293	prime full	medium	0.05817

to poorly influence data above 10keV and below 0.3-0.5 keV respectively. Because of this, only data between 0.5 and 10 keV were considered useful and all others was discarded.

Chapter 4

Tools for Data Analysis

4.1 Science Analysis Software

The information from the telescope itself was extracted using the Science Analysis Software (SAS). This software allows for data extraction and reduction from its original form, and generates spectra specifically from *XMM-Newton* data (The XMM-Newton ABC Guide, 2002).

4.2 Xspec

The spectra were analyzed using the high energy spectral fitting software, `Xspec`. This program allows the user to model spectra generated by any detector, which provides software for data analysis from any telescope. The basic idea of `Xspec` is that it allows the user to chose models to simulate the spectra, which can be manipulated using input parameters. The program computes the simulated spectrum and then compares it to the actual observed spectrum, while manipulating the parameters to produce the best fit.

4.3 Models

The spectra of the ULIRGs in the sample were modelled with a specific set of components simulating both AGN and starburst related emission. A total of seven features were used in multiplicative and additive modeling of the spectra. The multiplicative models used were ISM absorption in our galaxy (`tbabs`), red-shifted ISM absorption in the host galaxy (`ztbabs`), and both neutral and ionized partial covering around the X-ray source (`zpcfabs` and `zxipcf` respectively). The additive models used were a red-shifted blackbody spectra (`zbbody`), emission from a Mewe-Kaastra-Liedahl thermal plasma (`mekal`), a red-shifted photon power law (`zpowerlw`) and a red-shifted Gaussian line profile (`zgauss`), all of which deal with emission processes.

4.3.1 Tbabs & Ztbabs

The `tbabs` and `ztbabs` model ISM absorption according to the Tuebingen-Boulder absorption model (Xspec: An X-ray Spectral Fitting Package, 2012), both unred-shifted and red-shifted respectfully. The unred-shifted absorption, `tbabs`, was used to model the neutral hydrogen column density from our own Galaxy, while the red-shifted model was used to establish the absorption of the object in question. `Tbabs` was used for every galaxy modeled, but `ztbabs` was used only if it improved the fit. The only parameter for `tbabs` is the nH column density, which was found for the objects using the nH calculator from the Web-based Tools section of NASA's HEASARC website. The parameters for `ztbabs` are redshift and nH column density. In the case of `ztbabs`, the nH column density was left as a free parameter for the

objects in the sample, and the redshift was fixed to a known value.

4.3.2 ZPCFABS

The `zpcfabs` model deals with red-shifted absorption from a neutral medium partially covering the source (Xspec: An X-ray Spectral Fitting Package, 2012) (see Figure 4.1 for a geometric interpretation). The equation for the partial covering model is given by :

$$M(E) = fe^{-n_H\sigma(E(1+z))} + (1-f) \tag{4.1}$$

σ in this equation is the photoelectric cross-section excluding Thompson scattering. The input parameters are n_H in units of 10^{22} atoms cm^{-2}, the covering fraction, f, and the redshift. When modelling the ULIRGs, the redshift was fixed to a known value, and both n_H and f values where left free.

4.3.3 ZXIPCF

`Zxipcf` models red-shifted absorption by a partially ionized medium which is partially covering the source (Xspec: An X-ray Spectral Fitting Package, 2012) (see Figure 4.1). The input parameters are column density in units of 10^{22}cm^{-2}, log(xi), a covering fraction, and the redshift. The value of xi is given by equation 4.2.

$$xi = \frac{L}{nr^2} \tag{4.2}$$

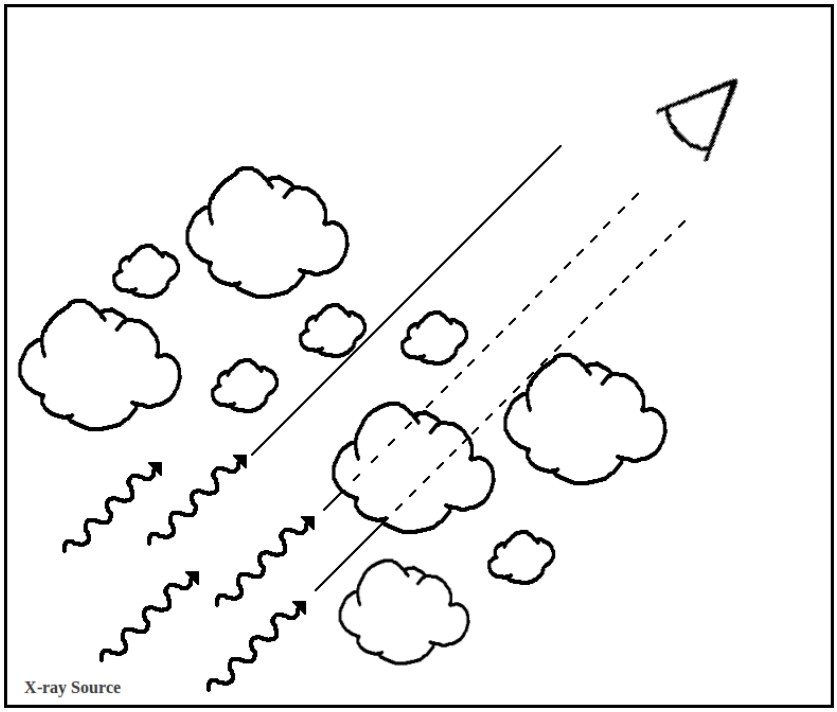

Figure 4.1: Partial Covering Model. In both the neutral and ionized partial covering models, a medium is partially obstructing the X-ray source. In these cases, the observer will see some of the direct light from the source and some light that has been absorbed and re-emitted by the medium in the direction of the observer. Much of the light through the medium will be scattered elsewhere.

In equation 4.2, L is the luminosity in units of ergs^{-1}, n is the number density of the plasma, and R is the distance from the ionizing source. Redshift was fixed to a known redshift for the objects in the sample, however the column density, covering fraction and log(xi) were left free.

4.3.4 ZBBODY

The `zbbody` model is a model of a red-shifted blackbody spectrum, and was used as a potential model for the soft X-ray spectra of the objects. A blackbody is a good indicator of an embedded AGN because of its connection to the soft excess seen in AGN spectra. What actually causes this emission is still highly debated today, with the most popular theory being ionized reflection from the inner accretion disk (Gierliski & Done, 2004). Although the physical nature of this emission is probably not actually blackbody emission, a blackbody models it well and was used in this study. The components of a ULIRG with an embedded AGN is shown in Figure 6.1 and and it's power law is displayed.

The spectrum is given by equation 4.3 (Xspec: An X-ray Spectral Fitting Package, 2012)

$$A(E) = \frac{8.052K\left[E\left(1+z\right)\right]^2 dE}{\left(1+z\right)kT^4\left[e^{(E(1+z)/kT)}-1\right]} \tag{4.3}$$

The input parameters for the model are kT, which is the temperature in units of keV, a fixed redshift, and a normalization, which is defined as:

$$K = \frac{L}{\left[D\left(1+z\right)\right]^2} \tag{4.4}$$

For equation 4.4, L is considered to be the source luminosity in units of 10^{39} ergs^{-1} and D is the distance to the source and is in units of 10 kpc. When using `zbbody` to model the ULIRG spectra, the redshift was set and fixed to a known redshift and the temperature and normalization were left as free parameters.

4.3.5 MEKAL

The `mekal` model is a model of a hot diffuse gas as defined by calculations made by Mewe, Kaastra and Liedahl (Xspec: An X-ray Spectral Fitting Package, 2012), and is used as a potential model for the soft X-ray spectra of the starburst objects. The `mekal` model specifically models plasmas which are collisionally excited, like those of galactic winds and supernova remnants (both abundant in star forming regions), meaning that it models X-ray emission of starburst galaxies. Both the continuum and emission lines are modeled using this model, and can be seen in Figures 6.2 and 6.3.

The input parameters for this model are kT, nH, abundance, redshift, switch and normalization. The kT parameter is the plasma temperature in units of keV, nH is the density in the plasma in units of cm^{-2}, abundance is the metal abundance with helium fixed at cosmic abundances, and normalization which is given by equation 4.5. The switch parameter allows the user to chose whether the model will be calculated using each temperature or interpolated from a pre-calculated table.

$$\frac{10^{-14}}{4\pi \left[D_A \left(1+z\right)\right]^2} \int n_e h_H dV \tag{4.5}$$

For equation 4.5, D_A is the angular diameter distance to the source in units of cm, n_e is the electron density, and n_H is the hydrogen density. When using `mekal` to model the spectrum, the switch parameter was set to 0 [1], redshift was fixed to a known redshift, and both abundance and nH were also fixed. The normalization and temperature parameters were left free.

4.3.6 ZPOWERLW

The `zpowerlw` model is a model of a simple red-shifted photon power law, and was used to model the hard X-ray spectra of the objects. The power law has different origins for both starburst dominated ULIRGS, and ones with an embedded AGN. The physics behind the power law emission is discussed in more detail in Chapter 1.3, but is produced by inverse Compton scattering in the corona by highly relativistic particles. The presence of the power law in starburst dominated galaxies is less clear, but one theory is that it originates in high mass X-ray binaries. This theory is discussed further in Chapter 8.1. The components of both AGN and starburst dominated ULIRGs are broken down in Figures 6.1, 6.2 and 6.3, and their power law components are shown.

The spectrum is given by equation 4.6(Xspec: An X-ray Spectral Fitting Package, 2012).

$$A(E) = K\left[E\left(1-z\right)\right]^{-\alpha} / \left(1-z\right) \tag{4.6}$$

[1]Setting the switch to zero calculated the model spectrum for each temperature using the Mekal code, rather than interpolating it from a table. While this is slower, it is a more accurate method (Xspec: An X-ray Spectral Fitting Package, 2012).

The input parameters for this model are α, which is the photon index of the power law, the redshift and the normalization, which is given by the number of photons per keV per cm^2 per second at 1 keV. The parameters were left open except for redshift, which was fixed to a known value for modelling the objects in the sample.

4.3.7 ZGAUSS

`Zgauss` is a simple red-shifted Gaussian model and is used to model emission lines, specifically the iron emission lines in the survey objects. For the modeled objects, `zgauss` modeled flourescent iron lines at 6.4, 6.7 and 6.97 keV, the former being a good indicator of an embedded AGN and the latter two hinting at starburst activity. The physics of the two are discussed in more detail in Chapters 1.3 and 1.4.

The Gaussian is modelled using equation 4.7(Xspec: An X-ray Spectral Fitting Package, 2012).

$$A(E) = \frac{K}{\sqrt{2\pi}\sigma^2\,(1+z)} e^{\frac{1}{2}[(E(1+z)-E_L)/\sigma]^2} \tag{4.7}$$

The parameters are E_l, σ, redshift, and the normalization. E_l is the line energy in units of keV, σ is the line width in units of keV and the normalization is the total number of photons per cm^2 per second in the line. The redshift was fixed to a known value, the line width was fixed to 0.001 keV and the line energies were set at either 6.4, 6.7 and 6.97 keV depending on which line was being modelled. The normalization was left free.

Chapter 5

Spectral Analysis and Classification

The spectral data were loaded into `Xspec` and the data which was considered bad were removed. All of the galaxies were first modelled from 2.0 to 10.0 keV with a red-shifted power law (`zpowerlw`) and then an intrinsically narrow Gaussian was added. An outline of the 2-10keV data for each object can be found in Table 5.1. Figure 5.1 shows the spectrum of Mrk 231 as an example of a modelled spectrum between 2.0-10.0 keV. It is modelled with a basic power law, and an emission line is present at 6.4 keV.

Not all spectra contained an emission line, however for the ones that did, the equivalent width of the line was found using the *eqwidth* `Xspec` command. The error in the equivalent width was found by calculating the error in the normalization of the Gaussian with the *err* command, and setting the lower error limit as a new parameter for the normalization. The model was re-fit, and the new equivalent width was calculated and used as the lower limit for the error. The upper limit for the error of the equivalent width was found using the same method, using the upper error limit from the normalization.

The value of the photon index should also have been an indicator of AGN or starburst activity. If the galaxy has an embedded AGN, it is expected that the power

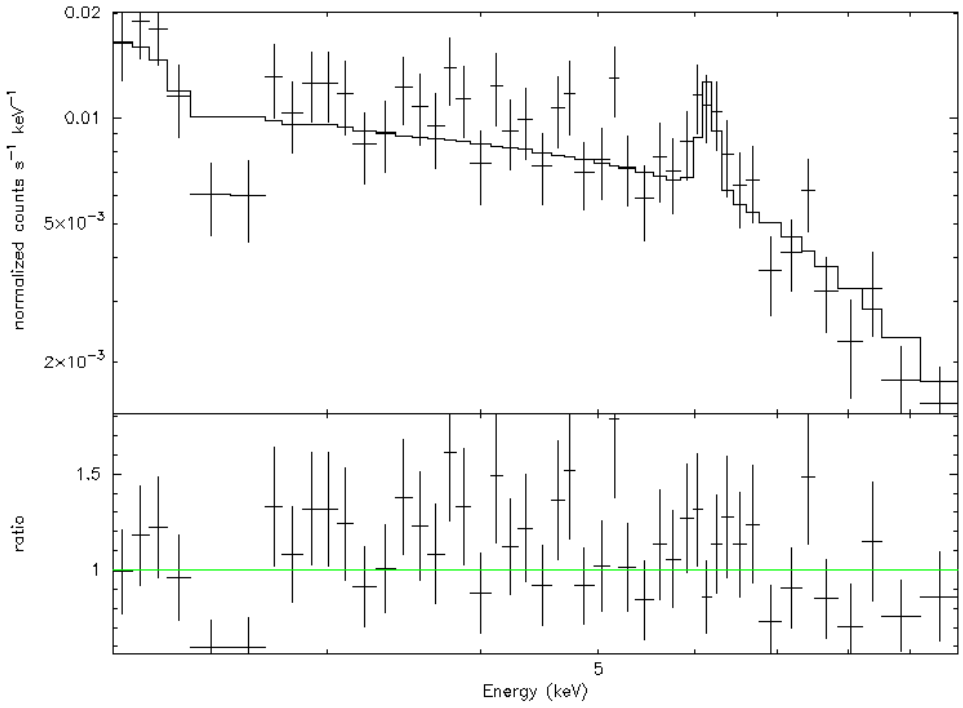

Figure 5.1: Modeled spectra of Mrk 231 between 2.0 and 10.0 keV

law will be quite flat, because of the AGN is highly extinguished, and therefor much of the power law emission is absorbed (Francschini et al., 2003). The starburst emission on the other hand, will be less absorbed as it originated from many points in the galaxy. This was not observed in the models used for these galaxies however, and the photon indexes shows no correlation between power source and power law absorption.

The spectra were then expanded to model the broad-band emission with either mekal or blackbody models. Each galaxy was modelled individually and both models were used separately to find the better fit. Along with the blackbody and mekal models, `ztbabs`, `zpcfabs` and `zxipcf` were all added to the spectra individually to improve the fit if necessary.

Table 5.1: Properties of the ULIRG Sample

Object	Γ^a	6.4 keV Eq. Width (keV)	6.7 keV Eq. Width (keV)	6.97 keV Eq. Width (keV)	L_{2-10} (10^{42}ergs^{-1})	nH (10^{22}cm^{-3})	χ^2_o
IRAS F05189-2524	2.12		$0.12^{+0.08}_{-0.08}$	$0.17^{+0.10}_{-0.10}$	22.2	5.04	1.22
IRAS F08572-3915	2.02				0.53		1.08
IRAS F10565+2448	2.42		$5.33^{+4.14}_{-4.36}$		0.17	1.08	0.96
IRAS F12112+0305	2.54				0.29	3.20	0.60
UGC 5101	3.95	$0.37^{+0.19}_{-0.19}$	$0.21^{+0.15}_{-0.14}$		0.59	0.48	1.04
IRAS F14348-1447	-1.16		$1.22^{+1.03}_{-1.03}$		1.16	0.44	0.77
IRAS F15250+3608	0.93				0.17	0.015	0.89
IRAS F22491-1808	9.34				0.02	0.60	0.83
Mrk 231	5.38	$0.22^{+0.12}_{-0.12}$			2.50	0.48	1.58
Mrk 273	-0.21	$0.32^{+0.12}_{-0.12}$	$0.28^{+0.12}_{-0.12}$		1.26	5.80	1.55
Arp 220	1.76		$2.31^{+0.90}_{-0.96}$		0.10		1.13

[a]Photon index of the power law.

5.1 IRAS F08572-3915

IRAS F08572-3915 was modelled from 2.0-10.0 keV using a red-shifted power law, and no emission lines were found. The power law had a photon index (Γ) of $2.02^{+0.62}_{-0.14}$. The broad-band spectrum was modelled using a red-shifted power law, a red-shifted blackbody and power law and a mekal and red-shifted power law. The best fit model was the mekal and red-shifted power law, which had a χ^2 of 38.8 per 36 degrees of freedom. The temperature of the mekal model was 79.89 keV. Figure 5.2 shows the model with the residuals plotted below. This object was classified as starburst dominated, and will be discussed further in Chapter 6.

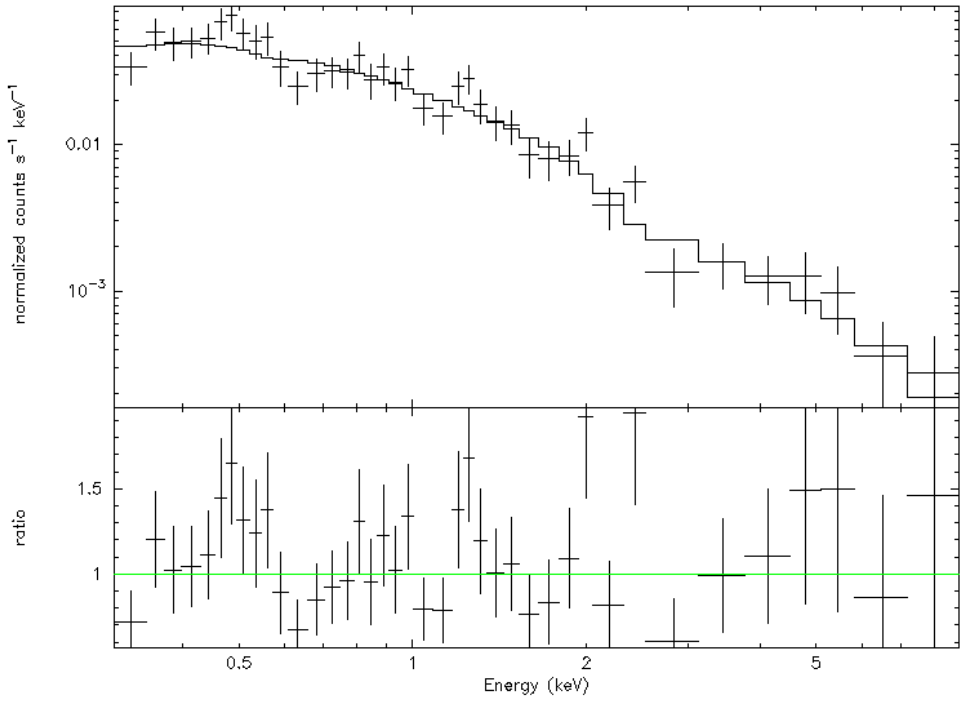

Figure 5.2: IRAS F08572-3915: Mekal and Power Law

5.2 IRAS F14348-1447

IRAS F14348-1447 was modelled from 2.0-10.0 keV using a red-shifted power law, and an emission line was found at 6.7 keV with an equivalent width of $11.22^{+1.03}_{-0.03}$ keV. Because the emission line is based on one data point and the uncertainties are so high, it was unclear whether this was an actual emission line. The photon index (Γ) of the power law was $-1.16^{+2.57}_{-1.27}$. The broad-band spectrum was modelled and the two best fits were that of an absorbed mekal and power law, and an absorbed blackbody and power law. The better fit, however, was the absorbed mekal and power law, which had a χ^2 of 21.50 per 28 degrees of freedom. The temperature of the mekal model was 3.18 keV and the nH column density in the object was 7.54×10^{20} cm^{-2}. Figure 5.3 shows the model with the residuals plotted below. This object was classified as

starburst dominated, and will be discussed further in Chapter 6.

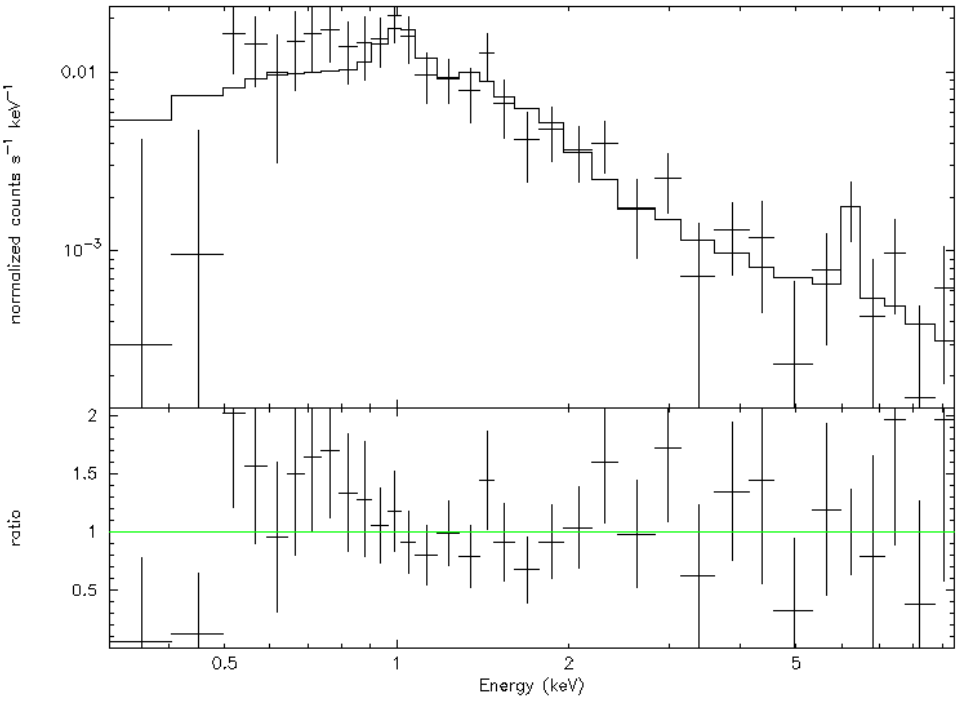

Figure 5.3: IRAS F14348-1447: Absorbed Mekal and Power Law

5.3 Arp 220

One of the interesting aspects of Arp 220 was that it had five separate spectra available. This allowed for the spectra to be stacked, so one spectrum with all of the data was created from the five individuals. The spectrum was modelled from 2.0-10.0 keV using a red-shifted power law, and an emission line was found at 6.7 keV with an equivalent width of $2.31^{+0.96}_{-0.90}$ keV. The photon index (Γ) of the power law was $1.76^{+0.15}_{-0.17}$. The broad-band spectrum was modelled and the best fit was the mekal and power law model, which had a χ^2 of 117.79 per 104 degrees of freedom. The temperature of the mekal model was 0.77 keV. Figure 5.4 shows the model with the

residuals plotted below. This object was classified as starburst dominated, and will be discussed further in Chapter 6.

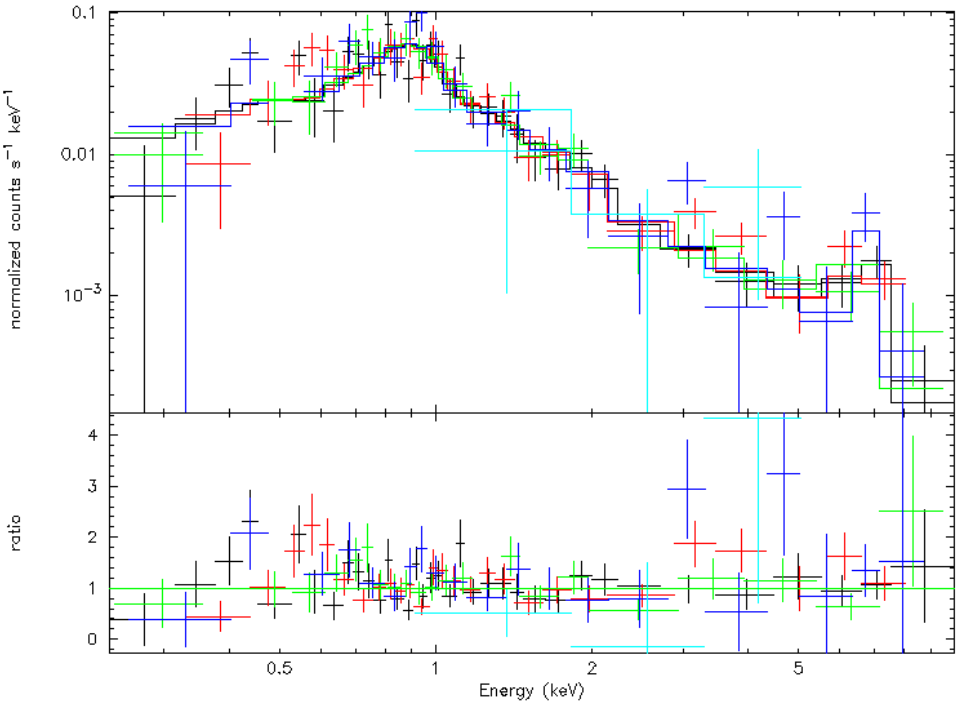

Figure 5.4: Arp 220: Mekal and Power Law

5.4 Mrk 231

Mrk 231 was modelled from 2.0-10.0 keV using a red-shifted power law, and emission lines were found at 6.4 keV with an equivalent width of $0.22^{+0.12}_{-0.12}$ keV. The photon index (Γ) of the power law was $5.38^{+0.92}_{-0.85}$. The broad-band spectrum was modelled and the two best fits were that of an absorbed mekal and power law, and an absorbed blackbody and power law. The better fit, however, was the absorbed blackbody and power law, which had a χ^2 of 165.83 per 105 degrees of freedom. The temperature of the blackbody was 2.10 keV and the nH column density in the object was 4.79×10^{21}

cm^{-2}. Figure 5.5 shows the model with the residuals plotted below. This object was classified as an AGN, and will be discussed further in Chapter 6.

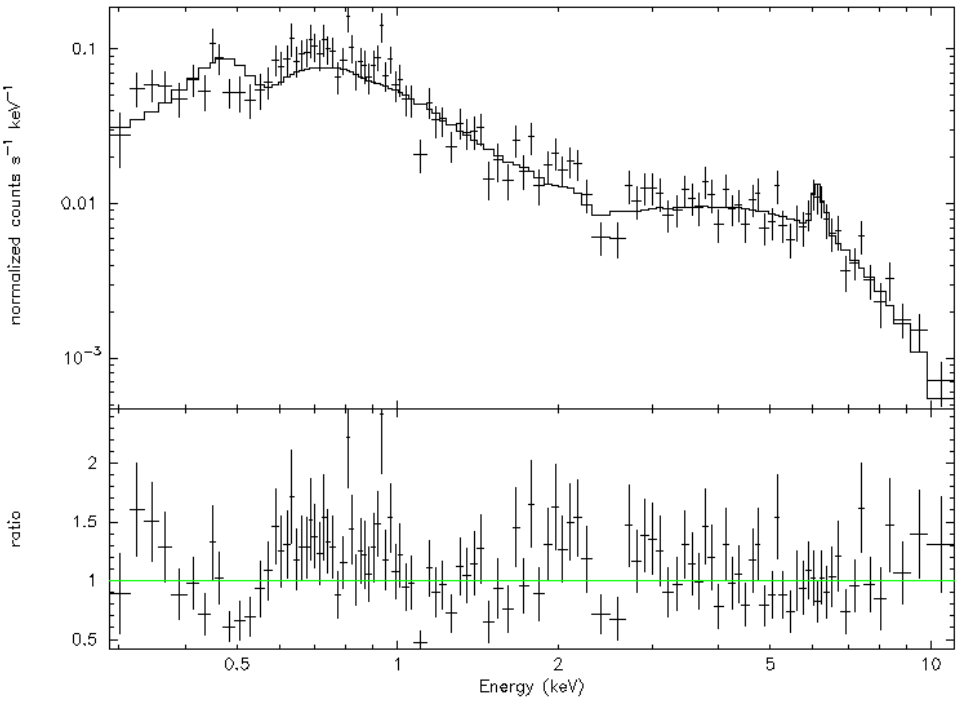

Figure 5.5: Mrk 231: Absorbed Blackbody and Power Law

5.5 IRAS F10565+2448

For IRAS F10565+2448, one emission line was found at 6.7 keV with an equivalent width of $5.33^{+4.14}_{-4.36}$ keV. Like IRAS F14348-1447, the line is dependent only on one data point, and the uncertainties are high. The photon index (Γ) of the power law was $2.42^{+0.45}_{-0.39}$. The broad-band spectrum was modelled and the best fit was that of a mekal and power law with a neutral partial covering. The model had a χ^2 of 34.67 per 36 degrees of freedom and the temperature of the mekal model was 0.65 keV. The cover fraction of the neutral partial covering model was 0.90 and the nH

column density in the object was 1.08×10^{21} cm^{-2}. Figure 5.6 shows the model with the residuals plotted below. This object was classified as starburst dominated, and will be discussed further in Chapter 6.

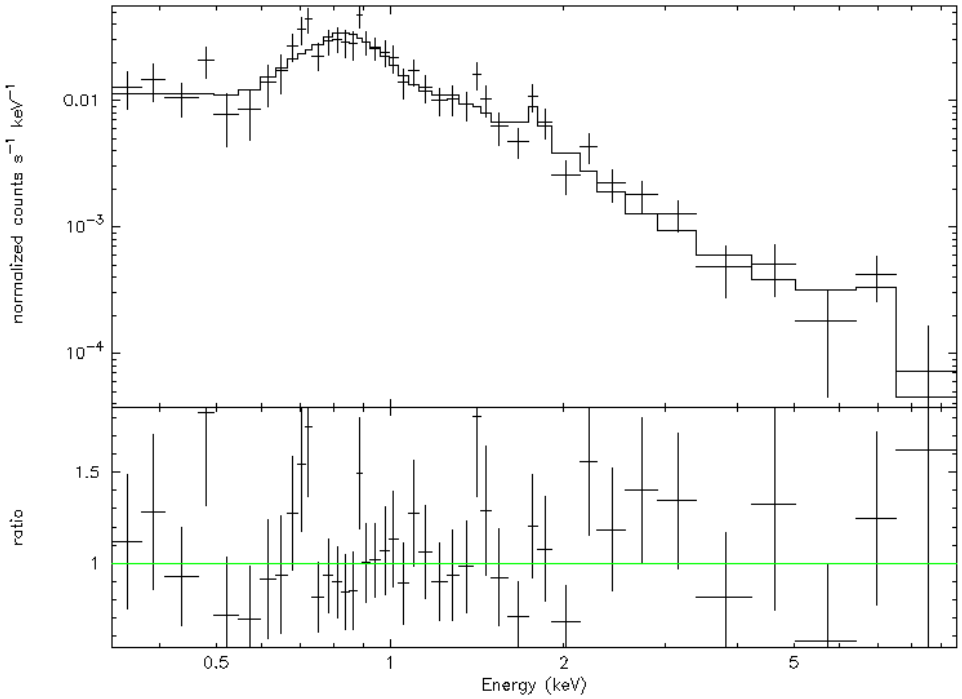

Figure 5.6: IRAS F10565+2448: Mekal and Power Law model with a Neutral Partial Covering

5.6 IRAS F15250+3608

IRAS F15250+3608 was unique in that it had very little data and therefore, fewer features could be significantly detected. It was modelled from 2.0-10.0 keV using a red-shifted power law, and no emission lines were found. The photon index (Γ) of the power law was $0.93^{+1.09}_{-1.16}$. The broad-band spectrum was modelled and the two best fits were that of an absorbed mekal and power law, and an absorbed blackbody and power law. The absorbed blackbody and power law underestimated the spectrum at

lower energies so the absorbed mekal and power law was the better fit. The model had a χ^2 of 9.75 per 11 degrees of freedom and the temperature of the mekal model was 0.33 keV and the nH column density in the object was 1.27×10^{18} cm^{-2}. Figure 5.7 shows the model with the residuals plotted below. This object was classified as starburst dominated, and will be discussed further in Chapter 6.

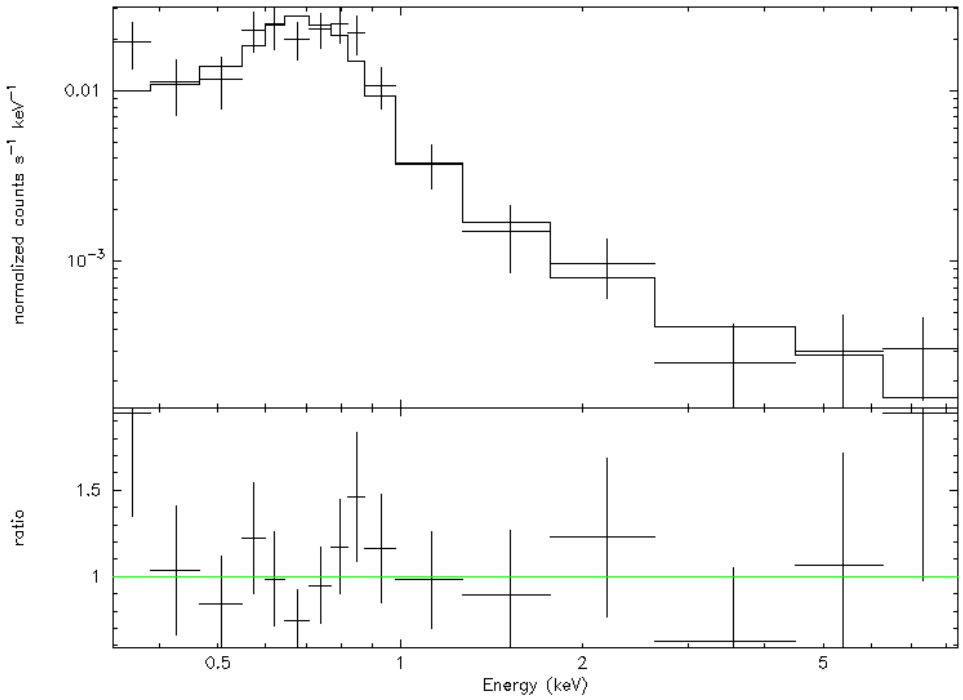

Figure 5.7: IRAS F15250+3608: Absorbed Mekal and Power Law

5.7 UGC 5101

Emission lines were found at 6.4 and 6.7 keV with equivalent widths of $0.37^{+0.19}_{-0.19}$ keV and $0.21^{+0.15}_{-0.14}$ keV respectively. The photon index (Γ) of the power law was $3.95^{+1.33}_{-1.06}$. The broad-band spectrum was modelled and the two best fits were that of an absorbed mekal and power law, and an absorbed blackbody and power law. The

absorbed blackbody and power law overestimated the spectrum at higher energies so the absorbed blackbody and power law was the better fit. The model had a χ^2 of 37.35 per 36 degrees of freedom and the temperature of the blackbody was 6.73 keV and the nH column density in the object was 4.75×10^{21} cm^{-2}. Figure 5.8 shows the model with the residuals plotted below. This object was classified as a combination of an AGN and starburst, and will be discussed further in Chapter 6.

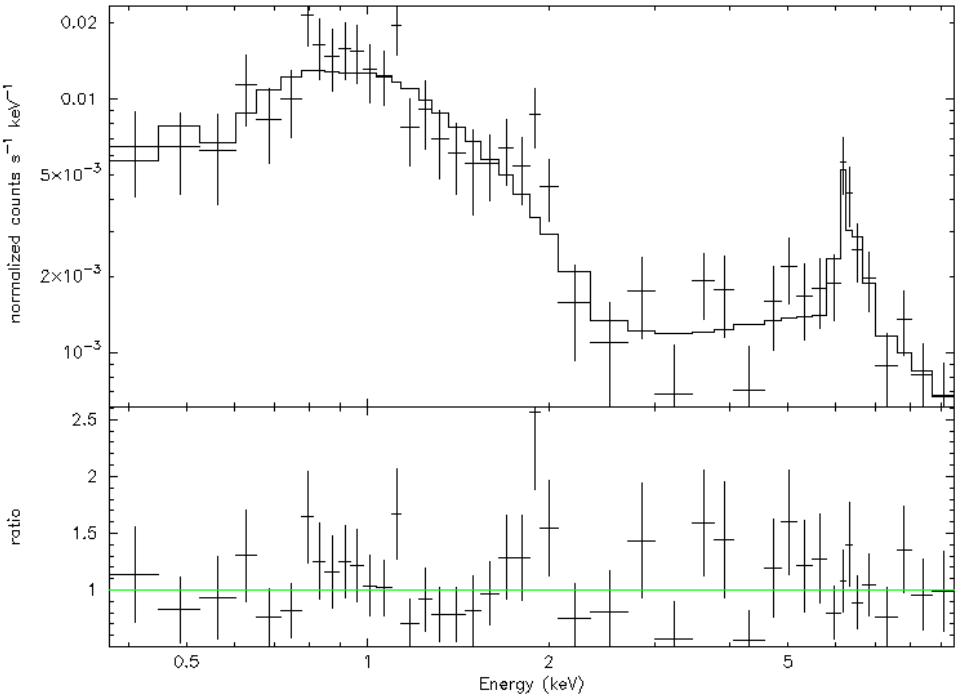

Figure 5.8: UGC 5101: Absorbed Blackbody and Power Law

5.8 IRAS F12112+0305

Similar to F15250+3608, IRAS F12112+0305 had very little data, and no emission lines were found. The photon index (Γ) of the power law was $2.54^{+1.11}_{-1.27}$. The broad-band spectrum was modelled and the best fit was that of a mekal and power law

with a neutral partial covering. The model had a χ^2 of 1.80 per 3 degrees of freedom and the temperature of the mekal model was 0.85 keV. The cover fraction of the neutral partial covering model was 0.90 and the nH column density in the object was 3.20×10^{21} cm^{-2}. Figure 5.9 shows the model with the residuals plotted below. This object was classified as starburst dominated, and will be discussed further in Chapter 6.

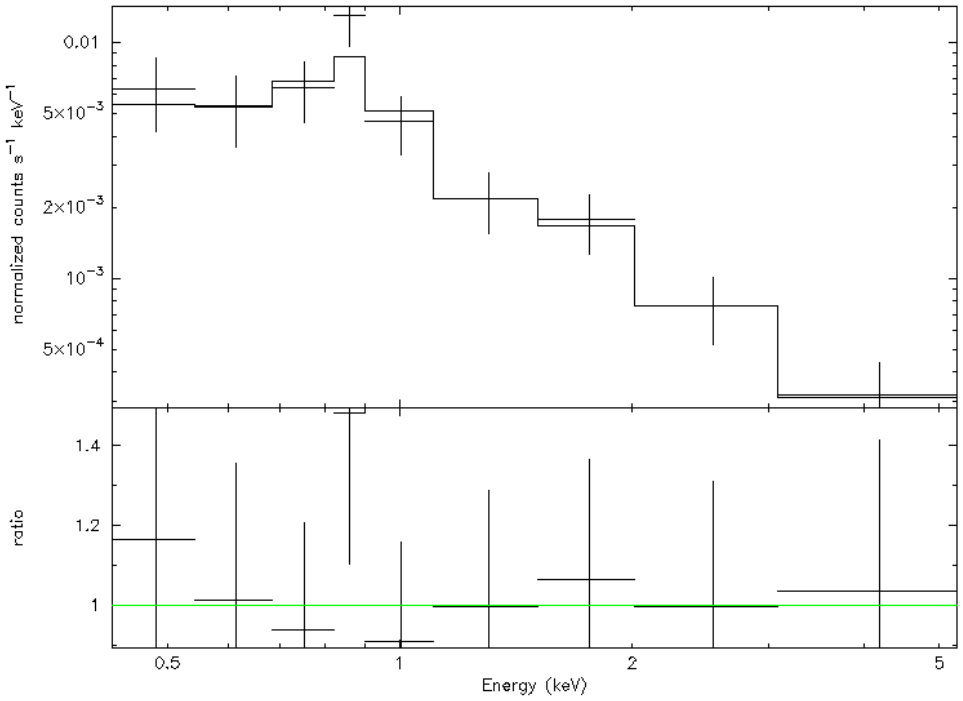

Figure 5.9: F12112+0305: Mekal and Power Law model with a Neutral Partial Covering

5.9 Mrk 273

For Mrk 273, emission lines were found at both 6.4 and 6.7 keV, with equivalent widths of $0.32^{+0.12}_{-0.12}$ keV and $0.28^{+0.12}_{-0.12}$ keV respectively. The photon index (Γ) of the power law was $-0.21^{+0.33}_{-0.35}$. The broad-band spectrum was modelled and the best fit

was that of a mekal and power law with a ionized partial covering. The model had a χ^2 of 95.80 per 62 degrees of freedom and the temperature of the mekal model was 0.65 keV. The cover fraction of the ionized partial covering model was 1.00 and the nH column density in the object was 5.79×10^{21} cm^{-2}. Log(xi) was found to be 2.08. Figure 5.10 shows the model with the residuals plotted below. This object was classified as a combination of an AGN and starburst, and will be discussed further in Chapter 6.

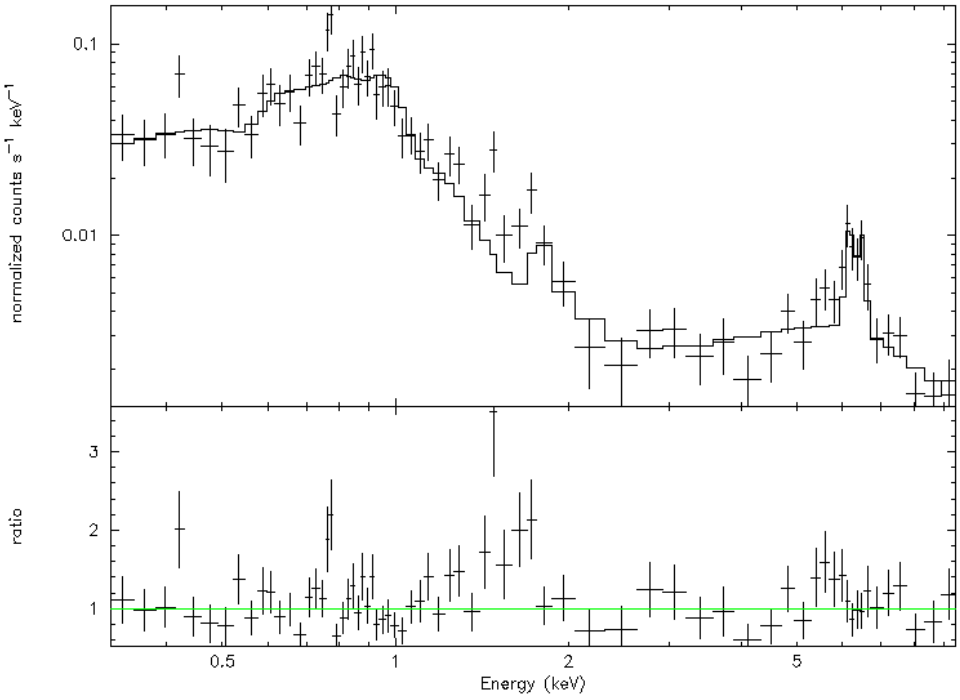

Figure 5.10: Mrk 273: Mekal and Power Law model with an Ionized Partial Covering

5.10 IRAS F22491-1808

No emission lines were found for IRAS F22491-1808 and the photon index (Γ) of the power law was $9.43^{+2.83}_{-1.02}$. The best fit model was that of an absorbed mekal and

power law which has a χ^2 of 8.29 per 10 degrees of freedom and the temperature of the mekal model was 0.65 keV. The nH column density in the object was 5.99×10^{21} cm^{-2}. Figure 5.11 shows the model with the residuals plotted below. This object was classified as starburst dominated and will be discussed further in Chapter 6.

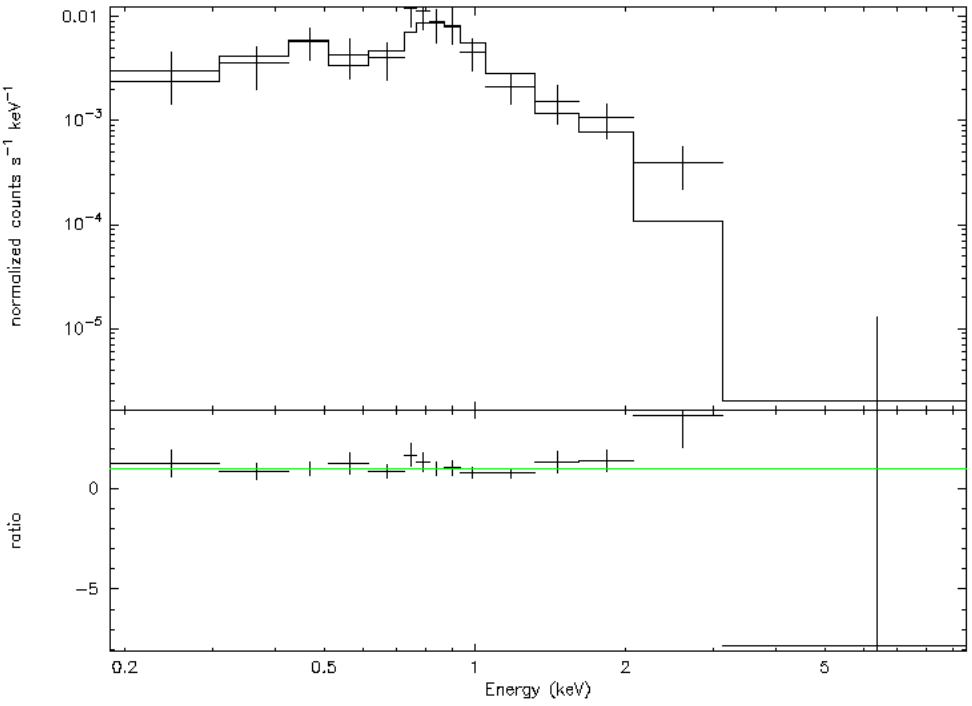

Figure 5.11: IRAS F22491-1808: Absorbed Mekal and Power Law

5.11 IRAS F05189-2524

IRAS F05189-2524 was probably the most unique and difficult galaxy to model. Both the absorbed mekal and power law and the absorbed blackbody and power law failed to model the spectrum well, so a more complex (and therefore less physical) model was adopted. The model that was used was that of an ionized partial covering of a mekal model with an individually absorbed power law. It should be noted however,

that this model is not unique, and probably does not fully explain the process of this galaxy.

Two emission lines were found for IRAS F05189-2524, one at 6.7 keV with an equivalent width of $0.12^{+0.08}_{-0.08}$ keV, and one at 6.97 with an equivalent width of $0.17^{+0.10}_{-0.10}$ keV. The photon index (Γ) of the power law was $2.05^{+0.03}_{-0.02}$ and the component had an nH column density of 5.82×10^{22} cm^{-2}. The temperature of the mekal model was 1.28 keV and it had an nH column density of 1.33×10^{24} cm^{-2}. The absorption of the mekal model also had a log(xi) of 2.75 and a covering fraction of 1.0. The model had a χ^2 of 163.29 per 134 degrees of freedom. Figure 5.12 shows the model with the residuals plotted below. This object was classified as an AGN and will be discussed further in Chapter 6.

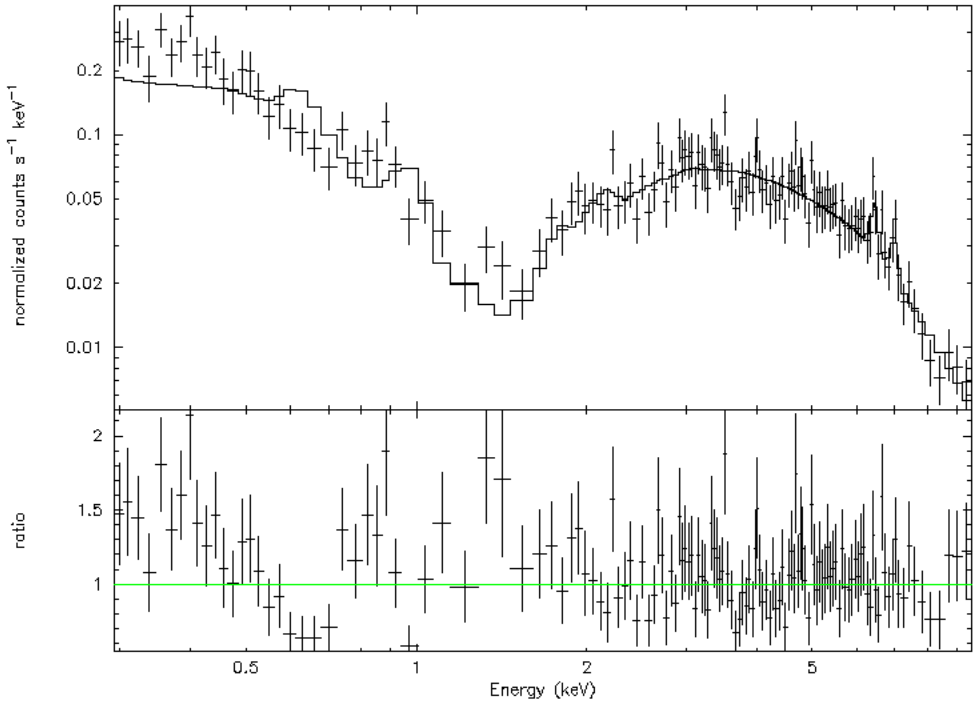

Figure 5.12: IRAS F05189-2524: Mekal With an Ionized Partial Covering and Absorbed Power law

5.12 Luminosity

The spectra were broken down into four parts to calculate luminosities. The first two luminosities calculated were that of the thermal component ($L_{thermal}$) and the power law component luminosity ($L_{powerlaw}$), and were both calculated between 0.5 and 10.0 keV. The luminosity of the entire spectrum was calculated between 0.5 and 2.0 keV ($L_{0.5-2}$), and between 2.0 ans 10.0 keV (L_{2-10}). All values were calculated using the *lumin* function in `Xspec`, which allows the user to determine the range of energies over which the luminosity is to be calculated and can be found in Table 5.2. This was trivial for calculating $L_{0.5-2}$ and L_{2-10}. For these values, all absorption was set to zero to ensure only the luminosity of the source was calculated, and then the *lumin* function was applied. Determining the values for $L_{powerlaw}$ and $L_{thermal}$ was slightly less straight forward. For these values, the component of the model for which the luminosity was not being found was negated for the spectrum by setting its normalization equal to zero. For instance, to calculate $L_{powerlaw}$ of a model consisting of a blackbody and power law, the normalization of the blackbody would be set to zero. The spectrum was left unfit with the zeroed normalization and any absorption was set to zero. The *lumin* function was then applied to the broad band spectrum.

Calculating the uncertainties of the luminosities was somewhat more difficult than calculating the luminosities themselves, and a "back-door" approach was adopted. To calculate the uncertainties, `Xspec`'s $cflux$ function was used. First the flux of either the model components or broad band spectra was calculated by adding the cflux component. The cflux tool is multiplicative and can therefore be combined with both

Table 5.2: Luminosities of the Model Components

Object	$L_{0.5-2}$ (10^{42}ergs^{-1})	L_{2-10} (10^{42}ergss^{-1})	$L_{thermal}$ (10^{42}ergs^{-1})	$L_{powerlaw}$ (10^{42}ergs^{-1})
IRAS F05189-2524	$29.02^{+0.06}_{-0.06}$	$22.26^{+0.03}_{-0.03}$	$11.47^{+0.16}_{-0.33}$	$39.14^{+0.06}_{-0.06}$
IRAS F08572-3915	$0.422^{+0.001}_{-0.001}$	$0.531^{+0.003}_{-0.04}$	$0.0190^{+0.0001}_{-0.0001}$	$0.531^{+0.039}_{-0.035}$
IRAS F10565+2448	$0.895^{+0.015}_{-0.019}$	$0.170^{+0.001}_{-0.001}$	$0.711^{+0.016}_{-0.032}$	$0.330^{+0.002}_{-0.003}$
IRAS F12112+0305	$0.761^{+0.020}_{-0.052}$	$0.293^{+0.005}_{-0.007}$	$0.411^{+0.014}_{-0.033}$	$0.642^{+0.017}_{-0.019}$
UGC 5101	$0.475^{+0.006}_{-0.007}$	$0.594^{+0.002}_{-0.003}$	$0.480^{+0.003}_{-0.04}$	$0.502^{+0.017}_{-0.099}$
IRAS F14348-1447	$2.23^{+0.01}_{-0.01}$	$1.17^{+0.01}_{-0.02}$	$1.71^{+0.02}_{-0.02}$	$0.132^{+0.003}_{-0.009}$
IRAS F15250+3608	$0.130^{+0.002}_{-0.006}$	$0.168^{+0.002}_{-0.004}$	$0.102^{+0.011}_{-0.064}$	$1.56^{+0.19}_{-0.44}$
IRAS F22491-1808	$2.22^{+0.03}_{-0.11}$	$0.0188^{+0.0003}_{-0.0004}$	$0.677^{+0.010}_{-0.19}$	$0.37^{+0.19}_{-0.19}$
Mrk 231	$3.64^{+0.02}_{-0.02}$	$2.50^{+0.6}_{-0.06}$	$2.46^{+0.01}_{-0.01}$	$3.58^{+0.09}_{-0.08}$
Mrk 273	$1.22^{+0.01}_{-0.01}$	$1.36^{+0.01}_{-0.01}$	$1.26^{+0.02}_{-0.02}$	$1.32^{+0.01}_{-0.01}$
Arp 220	$0.107^{+0.001}_{-0.002}$	$0.102^{+0.003}_{-0.004}$	$0.0485^{+0.0002}_{-0.0003}$	$0.141^{+0.005}_{-0.006}$

individual spectral components and the cumulative model. The spectra was fit, and a value for logarithm of the flux was obtained. Using the `Xspec`'s *err* function, the error of of the flux was also found. The percent error of the flux was then used as the percent error of the luminosity, allowing for values to be calculated.

Chapter 6

Classification

The method of classifying individual galaxies from their spectral components was adopted from Franceschini et al. (2003), and was composed of three criteria. If a galaxy was hosting an AGN, it would be expected to exhibit: a high luminosity from hard x-ray region of $L_{2-10} > 10^{42}\text{ergs}^{-1}$, a flat or inverted hard X-ray spectra and/or a strong Fe Kα emission line. If these were not present, the galaxy was assumed to be starburst driven. Along with the lack of AGN related features, starburst galaxies may also have highly ionized iron emission lines at 6.7 and 6.97 keV. The presence of mekal thermal emission was also linked to starburst activity, but was not a definitive factor.

Of the eleven objects, seven were classified as starburst driven and are outlined in Table 6.1. All of these galaxies were modelled with some combination of mekal and power law emission, and none showed signs of a 6.4 keV Fe Kα line. The only object classified as starburst driven which had a strong hard X-ray spectrum was that of IRAS F14348-1447, however, its mekal thermal emission and lack of 6.4 keV emission line lead to its starburst classification. Of the seven objects, three had a 6.7 keV iron line.

Two of the galaxies in the sample were classified as AGN. The first, IRAS F05189-2524, had a strong hard X-ray luminosity of $2.23\times10^{43}\text{ergs}^{-1}$, but did not display any

signs of a 6.4 keV emission line. This galaxy was still considered to be AGN dominated because of its luminosity between 2 and 10 keV, given its large nH column density (see Section 5.11). The other galaxy classified as an AGN was Mrk 231. This galaxy displayed both a high hard x-ray luminosity of $2.50\times10^{42}\text{ergs}^{-1}$ and a strong Fe Kα line at 6.4 keV.

The final two galaxies were classified as blended, showing features of both AGN and starburst activity. Mrk 273 had a hard x-ray luminosity of $1.36\times10^{42}\text{ergs}^{-1}$, putting it on the border being classified as AGN or starburst driven. While it contained a 6.4 keV emission line, it was not strong, and was accompanied by a 6.7 keV line as well and its thermal component was that of a mekal model. This combination of spectral features made it difficult to classify as one or the other, leading to the blended classification. Similarly, UGC 5101 displayed a weak hard x-ray luminosity of $5.95\times10^{41}\text{ergs}^{-1}$ but contained both a 6.4 and 6.7 keV emission line. Unlike Mrk 273, the thermal component of the model was a blackbody, which poses another question as to the galaxy's power source. Because of the low emission, but presence of a 6.4 keV iron line and thermal blackbody emission, UGC 5101 was also classified as a possible blended galaxy.

6.1 Model Components

The plots below show the component break down of a ULIRG classified as containing an AGN (Mrk 231), one dominated by starburst emission (Arp 220) and a blended galaxy (Mrk 273). Figure 6.1 shows the typical spectrum of an AGN embedded

Table 6.1: Classified Galaxies

Object	Classification
IRAS F05189-2524	AGN
IRAS F08572-3915	starburst
IRAS F10565+2448	starburst
IRAS F12112+0305	starburst
UGC 5101	blended
IRAS F14348-1447	starburst
IRAS F15250+3608	starburst
IRAS F22491-1808	starburst
Mrk 231	AGN
Mrk 273	blended
Arp 220	starburst

ULIRG with the hard power law (plotted in red), blackbody emission (blue) and an iron emission line at 6.4 keV. A typical starburst spetrum is seen in Figure 6.2 with a weaker power law, mekal emission (red) and an iron emission line at 6.7 keV. Figure 6.3 shows a blended galaxy with mekal emission in the soft X-ray region a strong power law and iron emission lines at 6.7 and 6.7 keV

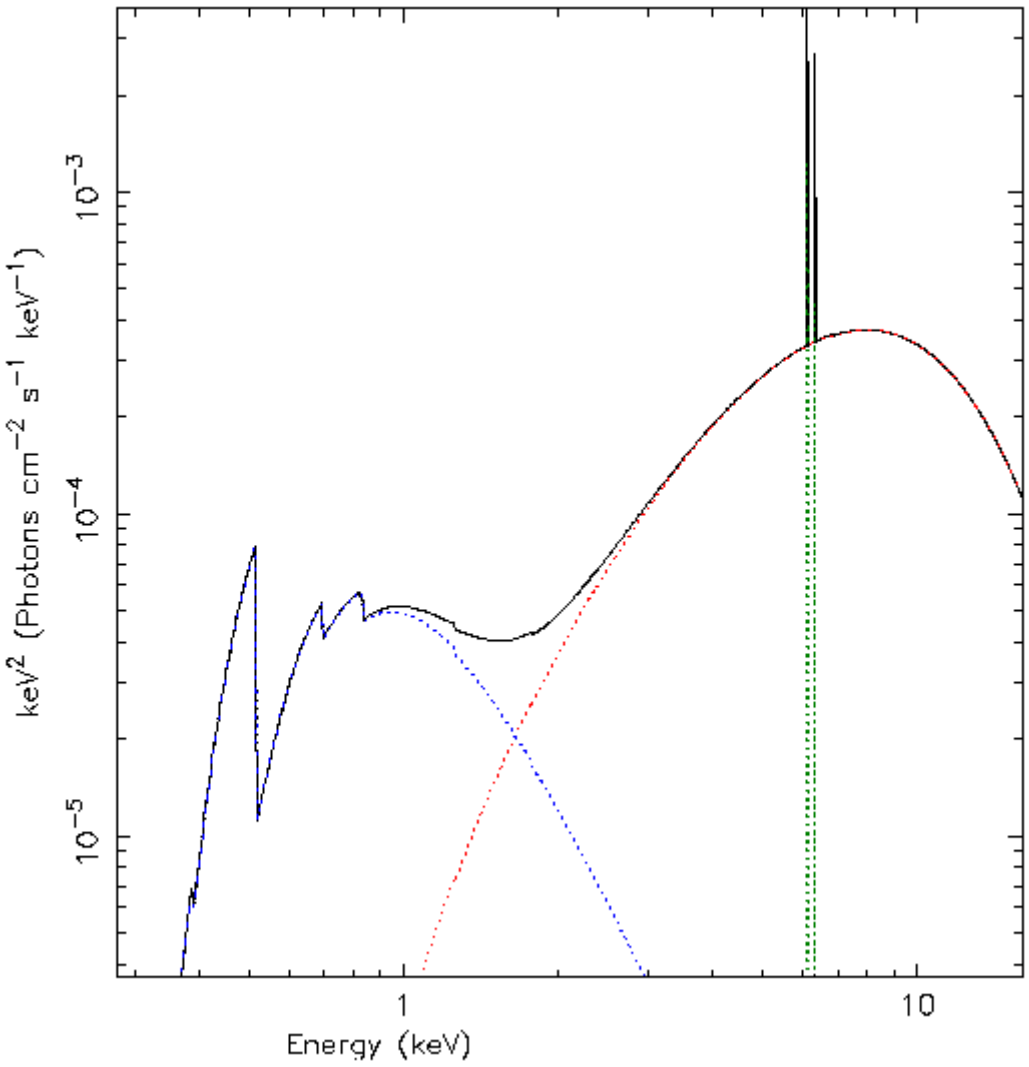

Figure 6.1: Mrk 231. Classified as containing an AGN, the components of the modeled spectra are shown. The power law is shown in red, the blackbody emission in blue, and the iron line in green.

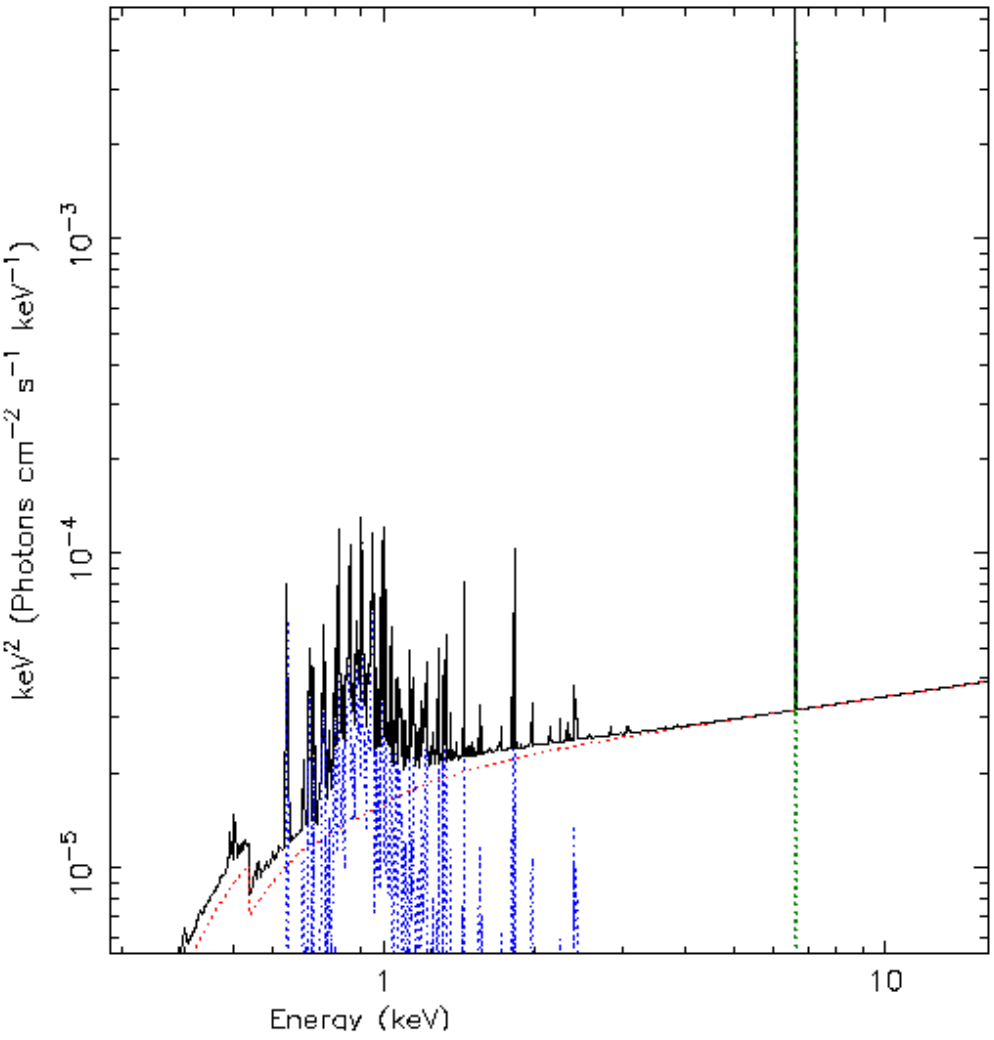

Figure 6.2: Arp 220. Classified as dominated by starburst emission, the components of the modeled spectra are shown. The power law is shown in red, the mekal emission in blue, and the iron line in green.

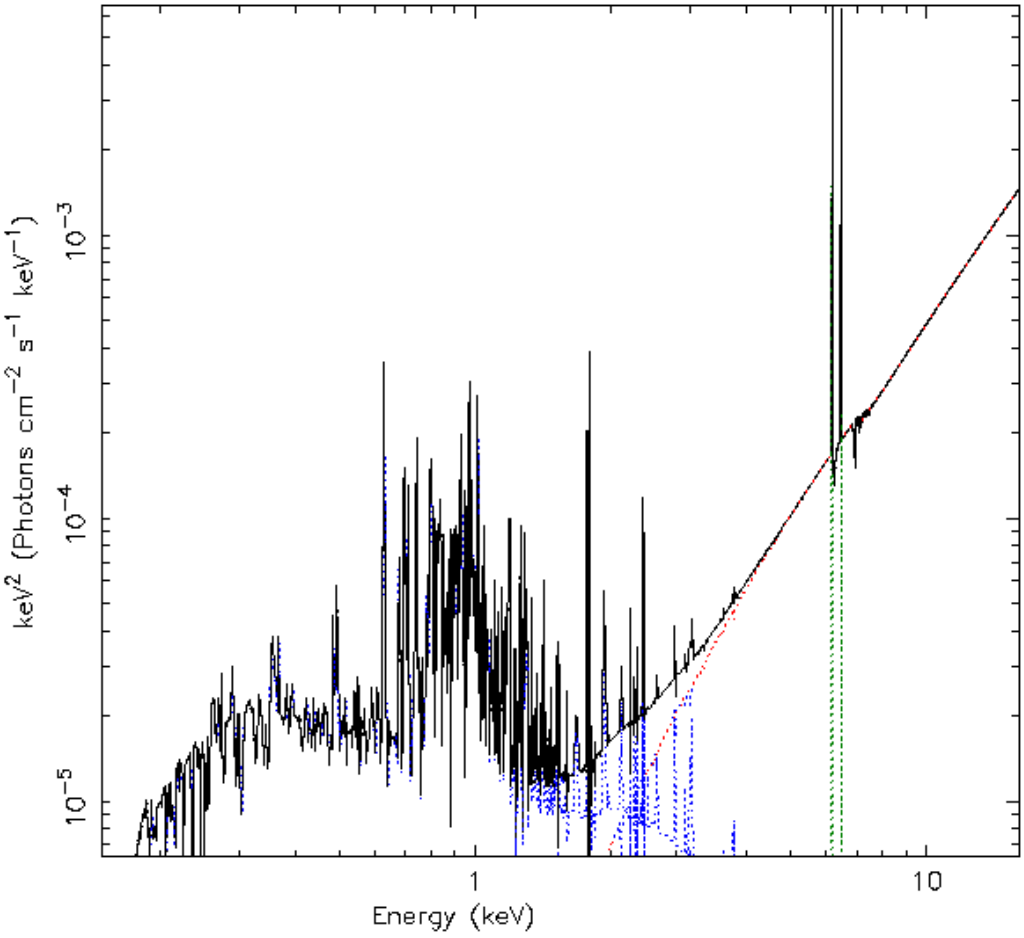

Figure 6.3: Mrk 273. Classified as blended, the components of the modeled spectra are shown. The power law is shown in red, the mekal emission in blue, and the two iron lines in green.

Chapter 7

Graphical Analysis

In addition to the spectral classification of each ULIRG, an analysis of the different best fit components was prepared. This allowed for observation of any trends in component luminosity as well as a comparison of the components to the infrared emission. Trends, both in component and infrared luminosity, can also be a good indicator for future classification of the objects, and can reveal potential correlations between emission processes.

7.1 Thermal and Power Law Luminosities

The broad-band luminosities between the thermal[1] and power law components were plotted in Figure 7.1. The AGN dominated ULIRGs are denoted by red squares, the starburst dominated ULIRGs are denoted by green circles and the ULIRGs considered to be blended are denoted by black diamonds. It is clear from the plot that the AGN, which are denoted by the red squares, have an excess in both power law and thermal emission as compared to the galaxies classified as starburst, denoted as green circles. The galaxies classified as blended, which are a combination of both AGN and starburst emission and are denoted by black diamonds, are located between the two

[1]Thermal emission here is considered to be either the blackbody or mekal components for the best fit models.

extremes, as expected. It may also be possible to see an excess in power law emission as compared to that of thermal emission for the Galaxies classified as AGN, however a larger sample of galaxies of this type would be needed to define a more convincing trend.

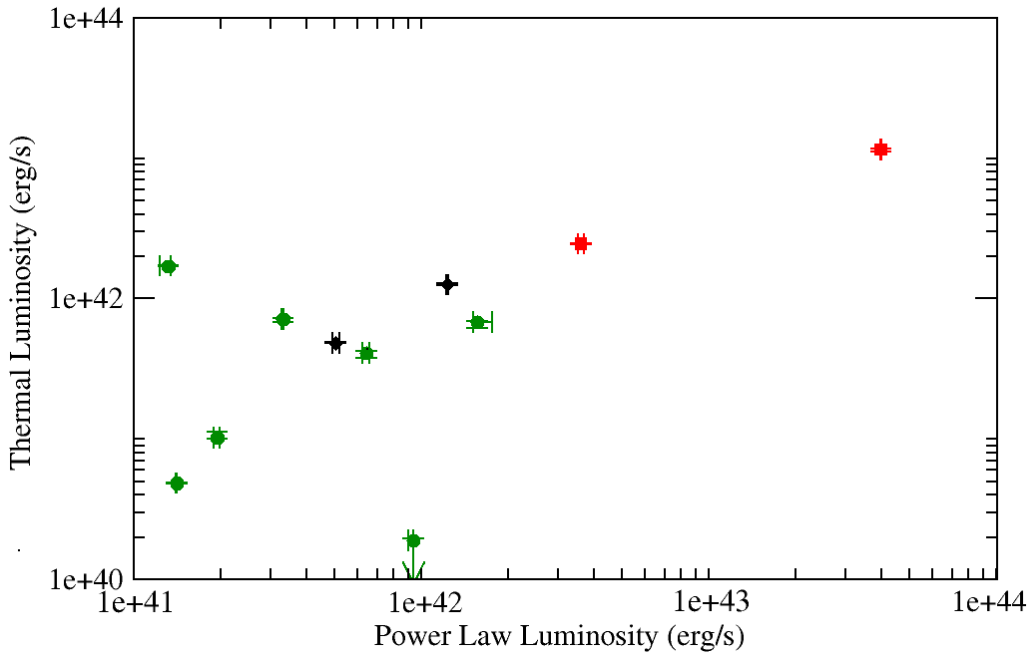

Figure 7.1: Best fit thermal and power law luminosities of classified ULIRGs. The red Squares represent AGN, the green circles represent starburst dominated galaxies and the black diamonds represent blended galaxies.

7.2 Infrared and power law luminosities.

The infrared and broad-band power law luminosities were plotted in Figure 7.2. It is clear with this plot that there is an excess in power law emission for a given infrared luminosity for the AGN dominated ULIRGs. As with Figure 7.1, the ULURGs classified as blended occupy somewhat intermediate positions between the AGN and starburst classified galaxies. However, ULIRGs dominated by starburst emission do

not seem to have well correlated infrared and power law emission, which is to be expected if they are dominated by thermal processes.

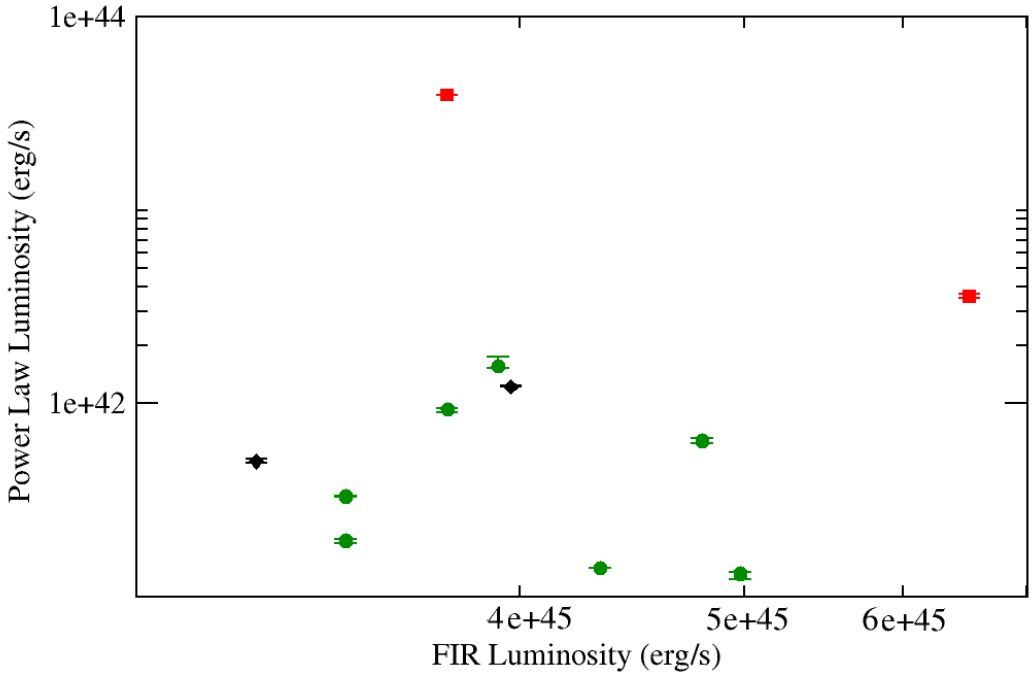

Figure 7.2: Infrared and power law luminosities of classified ULIRGs.

7.3 Infrared and Thermal Luminosities

The infrared and broad-band thermal luminosities were plotted against each other in Figure 7.3. Unlike in Figure 7.1, this plot shows no clear distinction between luminosities of either AGN or starburst driven galaxies. Although the AGN classified galaxies do show somewhat of an excess of thermal emission compared to that of the infrared emission, there is not enough of a difference to produce any definitive conclusions. Because both thermal X-ray and infrared emission are generally considered a good indicator of star formation (Francschini et al., 2003), this result at first seems odd. However, it may be explained by the idea that not all processes producing thermal

X-ray emission are caused by star formation. Other processes, like the density and pressure of the ISM may be contributing factors, and therefore influence the emission (Francschini et al., 2003).

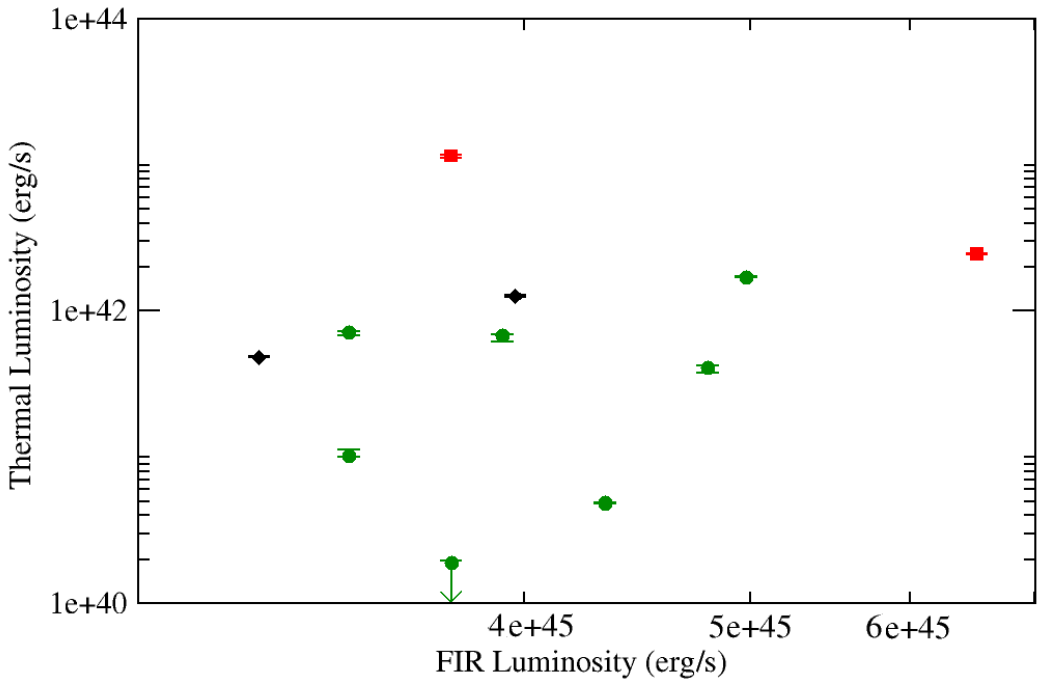

Figure 7.3: Best fit infrared and thermal luminosities of classified ULIRGs

7.4 Thermal and Power Law to Infrared Luminosity Ratios

Both the ratios of thermal emission and power law emission were plotted in Figure 7.4 to show the contributions of each. As with 7.1, there is a correlation between both thermal and power law emission in AGN dominated galaxies. In this case, the ratios of both thermal and power law luminosity to the infrared luminosity are higher than that of starburst galaxies.

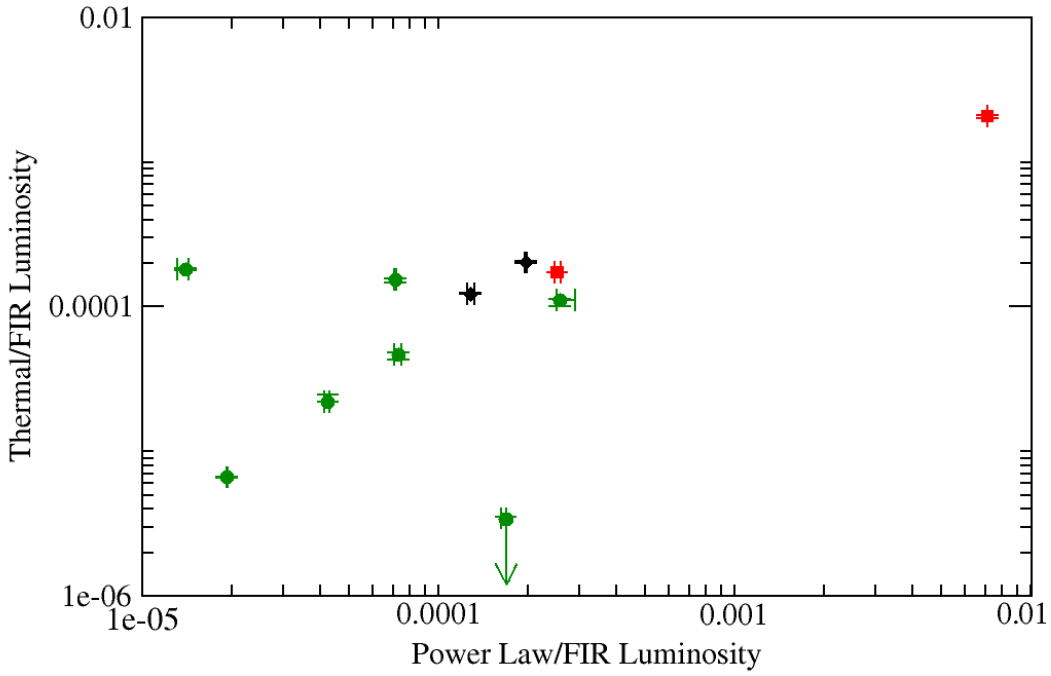

Figure 7.4: Infrared and thermal luminosities of classified ULIRGs.

Chapter 8

Hard X-ray Emission in Starburst Galaxies

One of the interesting aspects of the starburst galaxy spectra is the presence of power law emission in the 2.0-10 keV region. Power law emission is caused by either inverse Compton scattering in the halo of an active black hole with an accretion disk, or from synchrotron radiation produced by the jets of an AGN. The question then is: with little or no AGN activity in the host galaxy, what is the source of the hard X-ray power law emission? Because of their association with star forming galaxies, an abundance of high mass X-ray binaries are a probable cause of this emission (Robitaille & Whitney, 2010).

8.1 The Presence of High Mass X-ray Binaries

High mass X-ray binaries (HMXBs) are those which consist of a spectral type O or B star, orbiting a stellar mass black hole. As the black hole accretes matter from the companion, an accretion disk is formed, producing power law emission. HMXBs are associated with rapid star formation because the companion star is short-lived, meaning that rapid star formation would account for their presence in large numbers. If HMXBs are found to be present in the galaxies in large numbers, then they could account for the excess power law emission. This was determined using the

method adopted by Franceschini et al. (2003), who used the star formation rate of the associated galaxies and compared it to that of known local starburst galaxies.

8.1.1 Star Formation Rate

One of the intrinsic properties of any galaxy is the star formation rate (SFR), which can be determined in a number of different ways. Two independent methods of determining the SFR were used to investigate the presence of HMXBs in the galaxies. The first was derived from the object's far Infrared emission, and the second used the 2.0-10 keV X-ray emission.

Far Infrared emission is a good indicator of star formation because it is primarily caused by hot, short lived stars of spectral class 0 or B. The emission from these stars is re-radiated thermally by the surrounding dust, peaking in the infrared. The Infrared luminosity can therefor be used to calculate SFR using the following equation (Kennicutt, 1998):

$$SFR_{FIR} \simeq \frac{L_{FIR}}{2.2 \times 10^{43} ergs/s}(M_{\odot}/yr) \tag{8.1}$$

Likewise, X-ray emission can also be a good indicator because HMXBs, young supernova remnants and hot plasmas radiate in the X-ray region and are connected with rapid star formation. Unlike the thermal emission from young supernova remnants and hot plasmas, HMXBs radiate primarily in the 2-10 keV region. This means that an accurate SFR can be further narrowed to include only the HMXB contribution if they are the dominant source of emission in this range. Following Franceschini et al.

(2003), the equation for the 2-10 keV SFR was found by assuming that the Milky Way galaxy has a SFR of approximately $0.68 - 1.45 M_{\odot}/yr$ (Robitaille & Whitney, 2010) and hosts approximately 50 HMXBs (Iben, Tutukov & Yungelson, 1995) with mean luminosities of $L_{2-10keV} = 5 \times 10^{37}$ (White, Swank & Holt, 1983) The SFR estimate is then given by:

$$SFR_{X-ray} \simeq \frac{f \times L_{2-10keV}}{10^{39} ergs/s} (M_{\odot}/yr) \tag{8.2}$$

where f is a fraction that is determined by the contribution of HMXBs to the 2-10 keV emission. For starburst donated ULIRGs, f is assumed to be one.

The two star formation rates were plotted against each other in Figure 8.1. To provide further incite into the nature of starburst galaxies, the SFRs from a number of local, non-ULIRG starburst galaxies were added to the plot and are denoted by blue x's. The hard X-ray emission from these galaxies also have contributions from low mass X-ray binaries (LMBXs), and so equation 8.2 was used to calculate the SFR with f=0.25 (Francschini et al., 2003). X-ray and Infrared data for the local starburst galaxies was taken from papers by Dahlem et al. (1998) and Zezas et al. (1998), and Shapley et al. (2001) respectively.

As can be seen in Figure 8.1, the ULIRGs classified as starburst and the local non-ULRIG starburst galaxies follow a one-to-one ratio (dotted line) with the FIR emission based SFR. This means that both the accepted and assumed values agree, providing evidence of a HMXB contribution to the hard X-ray spectrum. As is expected, the galaxies classified as AGN fall above this line. This makes sense because the X-ray

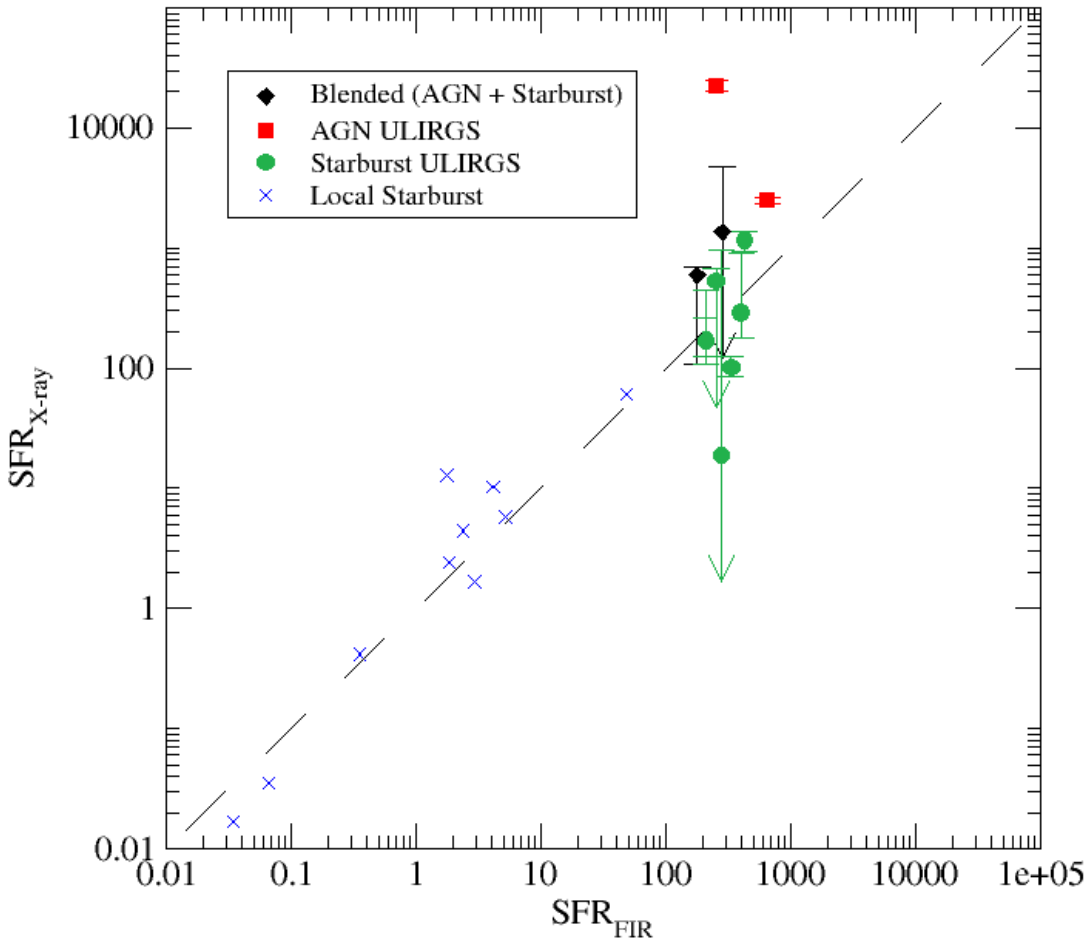

Figure 8.1: Infrared and power law star formation rates of local ULIRGs.

component of these galaxies is not based on star formation, and is by definition, stronger than that of starburst galaxies.

It is also interesting to note that the blended galaxies are consistent with the one-to-one ratio within uncertainties, although they lie slightly above it, showing that f is probably not equal to one in these cases. For these two galaxies, f was recalculated to force the objects to lie on the one-to-one ratio line. The value of f that would allow for this for both objects is f=0.3, which means that about one third of the power law component in these galaxies comes from high mass X-ray binaries, and the rest likely comes from an embedded AGN. .

Chapter 9

Summary

Of the eleven ULIRGs in the sample, all were able to be classified using their X-ray emission. The majority of the galaxies were found to be powered by starburst activity, with seven galaxies classified as starburst, two classified as hosting AGNs, and two considered to be blended, with contributions from both. This means that about 35% of the sample shows some form of AGN activity, which is consistent with results from other surveys of local ULIRGs. It also shows that, although starburst activity appears to be the dominant power source in the majority of ULIRGs, the contribution of AGN is still important.

The presence of high mass x-ray binaries was shown to be a probable contributor to excess power law in starburst galaxies. This is in agreement with a similar study by Francschini et al. (2003). This approach could be expanded however, to take a more in depth look at hard x-ray emission and what causes it, as it is unlikely there is only one contributor.

X-rays also appear to be a good indicator of star formation in starburst dominated ULIRGs. Although it is perhaps less precise in AGN because the luminosity has a different origin than star formation, accurate star formation sates of blended models can be found if the AGN contribution of hard X-ray emission is known.

This report could be improved upon in a few ways. A larger sample of ULIRGs

would provide a more varied and accurate look at the overall nature of the galaxies and allow for fewer statistical anomalies. Also, while the spectrum of the galaxy's X-ray emission was able to distinguish between starburst and AGN dominated power sources, it is important to note that a multi-wavelength approach would provide a more accurate look at the nature of these galaxies. Because the galaxies are X-ray dim, combining the X-ray data with a larger study including optical and sub-millimetre observations, might provide a better understanding of the hidden processes within.

Bibliography

Armus, L., et al. GOALS: The Great Observatories All-Sky LIRG Survey. *Astronomical Society of the Pacific*, 121:, 559-576, 2009.

Arnaud, K., Dorman, B. & Gordon, C. Xspec: An X-ray Spectral Fitting Package. *Users Guide"*, :, 2012.

Dahlem, M., Weaver, K. A., Heckman, T. M. An X-Ray Minisurvey of Nearby Edge-on Starburst Galaxies. I. The Data. *The Astrophysical Journal Supplement Series"*, 118:,401-453, 1998.

Desai, V. et al. PAH Emission from Ultraluminous Infrared Galaxies. *Astrophysical Journal*, 669:2810-820, 2007.

Farrah, D. et al. The Nature of Star Formation in Distant Ultraluminous Infrared Galaxies Selected in a Remarkably Narrow Redshift Range. *Astrophysical Journal*, 677:2957-969, 2008.

Francschini, A., et al. An XMM-Newton Hard X-ray Survey of Ultraluminous Infrared Galaxies. *Monthly Notice of the Royal Astronomical Society*, 343:1181-1194, 2003.

Gierliski, M,, Done, C. Is the soft excess in active galactic nuclei real? *Monthly Notice of the Royal Astronomical Society*, 349:17-11, 2004

Heckman, T. M., Lehnert, M. D., Armus L. Galactic Superwinds. *The Environment and Evolution of Galaxies*, 188:475, 1993.

Iben, I. Jr., Tutukov A. V., Yungelson L. R. A Model of the Galactic X-Ray Binary Population. I. High-Mass X-Ray Binaries. *Astrophysical Journal Supplement Series*, 100:217-231, 1995.

Kennicutt, R. C., Jr. The Global Schmidt Law in Star-forming Galaxies. *The Astrophysical Journal"*, 489:,451, 1998.

Lonsdale, C. J., Farrah, D., Smith, H. E. *Ultraluminous Infrared Galaxies*, *Astrophysics Update 2*. Praxis Publishing Ltd, Chichester, UK, 1st edition, January 2006.

Popp, M., et al. Performence of the pn-EPIC Detector aboard XMM. *Proceedings of the First XMM-Workshop on "Science with XMM"*, held at Noordwijk, The Netherlands, M. Dahlem (ed.):

Robitaille, T., Whitney, B. The Present-Day Star Formation Rate of the Milkey Way Determined from Spitzer-Detected Young Stellar Objects. *The Astrophysical Journal Letters*, 710:, 11-15, 2010.

Shapley, A., Fabbiano, G., Eskridge, P. B. A Multivariate Statistical Analysis of Spiral Galaxy Luminosities. I. Data and Result. *The Astrophysical Journal Supplement Series"*, 137:,139-199, 2001.

Snowden, S., Valencic, L., Perry, B., & Arida, M. The XMM-Newton ABC Guide: An Introduction to XMM-Newton Data Analysis. *"*:, 2002.

Strickland, D. K., Heckman, T. M., Weaver K. A., Dalhem, M. Chandra Observations of NGC 253: New Insights Into the Nature of Starburst-Driven Superwinds. *The Astrophysical Journal*, 120:2965-2974, 2000.

Vivian, U., et al. Spectral Energy Distribution of Local Luinous and Ultraluminous Infrared Galaxies. *The Astrophysical Journal Supplement Series*, 203:, 2012.

White, N. E., Swank, J. H., Holt, S. S. Accretion powered X-ray Pulsars. *The Astrophysical Journal*, 270:711-734, 1995.

XMM-Newton Users Handbook. *Issue 2.10* , 2012.

Zezas, A. L., Georgantopoulos, I., Ward, M. J. ROSAT and ASCA observations of X-ray luminous starburst galaxies: NGC 3310 and 3690. *Monthly Notices of the Royal Astronomical Society"*, 301:,915-925, 1998.